Oligocene-Early Miocene Topographic Relief Generation of Southeastern Tibet Triggered by Thrusting

Cao Kai, Guocan C Wang, Philippe Leloup, Gweltaz Mahéo, Yadong Xu, Pieter A van Der Beek, Anne Replumaz, Kexin Zhang

To cite this version:

Cao Kai, Guocan C Wang, Philippe Leloup, Gweltaz Mahéo, Yadong Xu, et al.. Oligocene-Early Miocene Topographic Relief Generation of Southeastern Tibet Triggered by Thrusting. Tectonics, 2019, 38 (1), pp.374 - 391. 10.1029/2017tc004832 . hal-03080776

HAL Id: hal-03080776
https://hal.science/hal-03080776v1

Oligocene-Early Miocene topographic relief generation of southeastern Tibet triggered by thrusting

Kai Cao [1, 2*], Wang G. C. [1, 2], Leloup P.H. [3], Mahéo G. [3],

Xu Y. D. [4, 5], van der Beek P.A. [6], Replumaz A. [6], Zhang K. X. [4]

[1] *School of Earth Sciences, Center for Global Tectonics, China University of Geosciences, Wuhan 430074, China*

[2] *State Key Laboratory of Geological Processes and Mineral Resources, China University of Geosciences, Wuhan 430074, China*

[3] *Laboratoire de Géologie de Lyon: Terre, Planètes et Environnement, Université Claude Bernard, 2 rue Daphaël Dubois, Villeurbanne 69622, France*

[4] *School of Earth Sciences, State Key Laboratory of Biogeology and Environmental Geology, China University of Geosciences, Wuhan 430074, China*

[5] *Key Laboratory of Sedimentary Basin and Oil and Gas Resources, Ministry of Natural Resources, Chengdu 610081, China*

[6] *Institut des Sciences de la Terre (ISTerre), Université Grenoble Alpes, CNRS, CS 40700, Grenoble 38058, France*

*Corresponding author: Kai Cao (kai.cao@cug.edu.cn)

Key Points:

- The Jianchuan basin experienced 2.3-3.2 km of exhumation at a rate of 0.57-0.80 km/Myr at ~28-20 Ma.
- Exhumation of the Jianchuan basin was accomplished prior to *ca.* 20 Ma.
- Topographic relief in southeastern Tibet is partly produced by thrusting along the Yulong thrust belt during the Oligocene-Early Miocene.

Abstract

The timing and mechanisms of uplift in southeastern Tibet remain disputed. To address this debate, we conducted structural and morphological analyses of the Yulong thrust-belt; we also reconstruct the cooling and exhumation history of the Jianchuan basin in the hanging wall of the thrust system using inverse thermal modeling of apatite fission-track and (U-Th)/He thermochronology data. Our results provide evidence for 2.3-3.2 km of rapid exhumation in the Jianchuan basin between ~28 and ~20 Ma, followed by limited exhumation of less than 0.2 km since then. The magnitude of basin exhumation is consistent with the present-day topographic step of 1.8-2.4 km across the Yulong and Chenghai thrust belts, as shown by morphometric analysis. We thus infer that the present-day morphology of the southeastern margin of Tibet results partly from thrusting along the Yulong thrust belt during the Late Oligocene-Early Miocene. This structure may be the southwest continuation of the Longmen Shan thrust belt, offset by the Xianshuihe fault in the Late Miocene. On a regional scale, the approximate synchronicity of exhumation in the hanging walls of the Yalong-Yulong and Longmen Shan thrust systems indicates that widespread crustal shortening and thickening took place in southeastern Tibet during the Late Oligocene-Early Miocene.

1 Introduction

Southeastern Tibet is characterized by widespread high-elevation (≥4000 m a.s.l.), low-relief surfaces (Clark et al., 2005a; Liu-Zeng et al., 2008) and a transition towards lower elevations in the southeast (Figure.1A). Understanding the origin of this landscape is critical to decipher between two end-member models for the tectonic evolution of this area: block extrusion (e.g., Tapponnier et al., 1982, 2001) and lower crustal flow (e.g., Royden et al., 1997; Clark and Royden, 2000). The former model predicts large-scale lateral block escape along major strike-slip faults together with crustal shortening on the margins of the plateau, while the latter foresees distributed crustal thickening in the plateau interior followed by propagation of the high altitudes toward the southeast, resulting in a continuous gentle topographic slope. In addition, other models emphasize that a significant part of the topography may be inherited from crustal deformation prior to the India-Asian collision (e.g., Kapp et al., 2007; Rohrmann et al., 2012). The temporal and spatial links between crustal deformation (i.e., shortening) and building of topography are thus key to distinguish between these competing models.

The timing of topographic growth of southeastern Tibet remains controversial. Incision of the Jinsha-Yangtze River and its major tributaries, dated at ~13-9 Ma by low-temperature thermochronology, has been interpreted as a proxy for the onset of uplift driven by lower crustal flow (Clark et al., 2005a; Ouimet et al., 2010). However, much older incision ages of ~22-15 Ma and ~18-9 Ma recorded by low-temperature thermochronology (Tian et al., 2014) and cosmogenic nuclides (Mcphillips et al., 2015) have been proposed for the paleo-Jinsha River, suggesting that the pattern of uplift may be more complex. Moreover, it has recently been proposed that Mid-Miocene river incision in southeastern Tibet may respond to a climatic rather than a tectonic-uplift trigger (Nie et al., 2018). Stable-isotope paleoaltimetry results indicate that western Yunnan probably attained its present-day elevation of ~3.3 km in the Late Eocene (Hoke et al., 2014). Paleoaltimetry data from the Shuanghe Formation (Fm.) in the Jianchuan basin were initially interpreted to indicate that the basin had reached an elevation of ~2.6 km in the Early Miocene (Li et al., 2015). However, Gourbet et al. (2017) have subsequently demonstrated that the Shuanghe Fm. is in fact Late Eocene in age, and re-evaluated the same data to indicate a lower elevation of ~1.2 ± 1.2 km at that time.

Since the Eocene, southeastern Tibet has been affected by the Oligocene-Miocene Ailao Shan-Red River (ASRR) left-lateral shear zone, the kinematics of which is well documented (Leloup et al., 1995, 2001; Replumaz et al., 2001; Figure 1): 700±200 km of initial left-lateral offset were followed by reversal to right lateral strike-slip as the Red River fault system. Although local uplift/exhumation along the ASRR may be linked to these kinematics (Leloup et al., 2001), they do not provide a viable mechanism for regional uplift of southeastern Tibet as the fault strikes perpendicular to the topographic margin. Thus, regional uplift is attributed either to lower-crustal channel flow (Schoenbohm et al., 2006), or to crustal thickening along several thrust systems, such as the Yulong thrust belt (YTB), Muli thrust, Jinghe-Qinhe thrust belt (JQTB) and Chenghai thrust (CHT) (Liu-Zeng et al., 2008; Perrineau, 2010; Figure 1). However, the kinematics of these thrust belts and their relationships with exhumation and relief production are still poorly constrained.

In this paper, we reconstruct the cooling and exhumation history of the Jianchuan basin, located in the hanging wall of the YTB, using inverse thermal modeling of apatite fission-track (AFT) and (U-Th)/He (AHe) thermochronology data. These results enable us to link significant relief generation of southeastern Tibet during the Oligocene-Early Miocene to regional thrusting in the context of crustal compression.

2 Geological setting

Southeastern Tibet is divided into several tectonic blocks (e.g., the Chuandian and Indochina blocks) by large-scale strike-slip faults (Figure 1A). Its high-elevation plateau topography is dissected by a distinctive parallel, southeast-flowing river network. Along the eastern plateau margin, the Longmen Shan represents a steep topographic barrier adjacent to the Sichuan Basin and records two major phases of exhumation, from ~30 to 25 Ma and ~15 to 10 Ma, respectively (E. Wang et al., 2012). The earlier episode of exhumation is interpreted to be related to thrusting along the Longmen Shan thrust belt (E. Wang et al., 2012). In contrast, Miocene exhumation of the Longmen Shan has been linked to similar cooling phases in southeastern Tibet (Figure 1A) and has been interpreted to be related either to lower-crustal flow (Clark et al., 2005a; Ouimet et al., 2010) or to continued thrusting.

To the southwest of the Longmen Shan, across the Xianshuihe left-lateral strike-slip fault, the margin of the plateau corresponds to the Yalong-Yulong thrust belt comprising the Muli, Yulong, Chenghai and Jinhe-Qinghe thrust belts (Figure 1). This fault system coincides with a series of topographic steps along which elevation decreases from ~4.2 km to ~1.8 km over a distance of 200-250-km (Liu-Zeng et al., 2008). The Muli thrust and JQTB were interpreted to represent the southward continuation of the Longmen Shan thrust belt (Wang et al., 1998) and thus to have possibly accumulated a few tens of kilometers of shortening during Oligocene-Miocene times (Burchfiel et al., 1995), which may have induced ~2 km of surface uplift (Clark et al., 2004). Based on geological cross sections, Perineau (2010) estimated ~12 km of Cenozoic shortening across the JQTB and ~3.5 km of uplift in its hanging wall. For the Muli thrust, Cenozoic shortening is estimated at ⩾22.5 km and the magnitude of uplift at ~3.5 km (Perrineau, 2010). AFT data interpreted to come from the hanging wall of the JQTB revealed an increase of the apparent exhumation rate at 17±2 Ma, which was interpreted to be related to initial thrusting while the fault presumably acted as a transpressive termination of the Xianshuihe fault (S. Wang et al., 2012). Others have proposed that the Xianshuihe fault in this area initiated at ~9 Ma, and displaced former thrusts by ~60 km (Zhang et al., 2017). The N-S-striking Yulong and Chenghai thrusts crosscut Eocene deposits (BGMRY, 1990), and thus postdate the Eocene. About 20 km west of the YTB, the Yulong anticline lies in the hanging wall of the fault, with a fold axis parallel to the fault (Figure 2). A ^{40}Ar/^{39}Ar K-feldspar plateau age from a mica-schist sample suggests that folding took place at ~17±3.5 Ma (Lacassin et al., 1996).

These folds and thrusts are affected by N-S striking active normal faults that bound Pliocene-Quaternary basins (Figure 2). These faults constitute the Lijiang pull-apart system between the active Zhongdian and Red River faults (Leloup et al., 1995). The YTB and CHT are not found across the Red River fault, which roughly follows the trace of the Oligocene-Miocene ASRR (Figure 1A). The onset timing for sinistral shearing of the ASRR remains debated, ranging from ~34 to 28 Ma (Cao et al., 2011; Leloup et al., 1995, 2001; Palin et al., 2013). Left-lateral shear probably ceased at ~17 Ma (Leloup et al., 2001). Reactivation of the Red River fault in a dextral sense occurred at ~10-5 Ma and ~25 km offset has accumulated since then (Leloup et al., 1993; Replumaz et al., 2001).

The Late Eocene Jianchuan basin is bounded by the Qiaohou thrust belt to the west and the Jianchuan fault to the east (Figures 2 and 3). Thrusting along the Qiaohou thrust belt induced folding of the basin interior in the Late Eocene or later (Gourbet et al., 2017). In contrast, the Jianchuan fault, part of the Red River fault system, probably initiated in a normal sense synchronous with dextral strike-slip of the main fault in the Late Miocene (Leloup et al., 1995; Replumaz et al., 2001), which likely controls the Pliocene-Quaternary Dianwei pull-apart basin (Leloup et al., 1995; Wang et al., 1998). The Jianchuan basin contains >5.5 km of Paleogene fluvial-lacustrine and volcanic deposits (Figures 2 and 3) and records intensive magmatism at ~35-36 Ma (Gourbet et al., 2017; Lu et al., 2012). Robust zircon U-Pb geochronologic dating on igneous rocks crosscutting the lower part of the Paleogene fluvial-lacustrine sediments (i.e., E_1m, E_2b, E_2jz) and interstratified within the upper part of the Paleogene volcanic sediments (i.e., E_2s, E_2jc) indicates that the Cenozoic formations within the basin are mostly Eocene in age, and particularly that Oligocene-Miocene sediments are absent (Gourbet et al., 2017; Figures 2 and 3).

3 Structural and morphometric analysis

3.1 The Yulong thrust belt (YTB)

The YTB consists of several branches and runs for over ~160 km from south of Heqing to the east of the Yulong Xue Shan range (Figure 2A). The fault trend changes from NNE-SSW in the south to N-S in the north (BGMRY, 1990; Figure 2A). The southern portion of the main fault extends along the eastern margin of the Heqing basin and has been locally obscured by later normal faulting. Structural investigation at five sites (JC46, CD101, CD305, CD306 and CD357; Figure 2) allowed us to characterize the kinematics of these brittle faults. At sites CD101, CD305 and CD357, the fault-damage zone is characterized by intense brittle deformation, with unsolidified to semi-solidified fault breccias and cataclasite (Figures 4A and 4B). The thrust faults strike NNE-SSW and dip between 35 and 80° to the west (Figures 2B and 2C). The lense-shaped breccias, fractures and slickensides in the fault zones indicate reverse motion with a minor strike-slip component (Figures 2B, 2C, 4C, 4D and 4E). At a larger scale, the principal fault of the YTB is a thrust that locally places Triassic sediments over Eocene conglomerates equivalent to the basal rocks of the Baoxiangsi Fm. (E_2b) in the Jianchuan basin (Figures 4C and 4E). Another possible splay of the YTB brings Permian basalts and Paleozoic metamorphic rocks on top of Triassic sediments between the Heqing and Jianchuan basins (Figures 2A and 2E).

In the north, the Yulong anticline is located in the hanging wall of the YTB, ~20 km west of the main thrust. Its fold axis trends N 175° (Lacassin et al., 1996), parallel to the thrust, suggesting that these two structures are genetically related. The timing of folding is estimated to be 17±3.5 Ma (Lacassin et al., 1996). Within the Jianchuan basin, Gourbet et al. (2017) have shown that Late Eocene sediments of the Shuanghe (E_2jc) and Jiuziyan Fms. (E_2jz) are folded with an axis trending N 7°, parallel to the YTB (Figure 2A). To the east of the Pliocene-Quaternary Heqing basin, Eocene conglomerates are crosscut by the NNW-trending thrust faults of the YTB (Figures 3C, 3D and 4). Geological mapping shows a Triassic sliver lying on top of the Eocene in that area (BGMRY, 1990; Figure 2). These observations imply that the YTB initiated after the Late Eocene (~35 Ma). The YTB thrusts are cut by steep N-S-striking normal faults bounding the Pliocene-Quaternary Heqing basin to the east (Figures 2A, 2D, 2E and 3). Assuming that these normal faults initiated at ~5 Ma, as suggested by the timing of onset of the Dali normal fault located 90 km south of Heqing (Leloup et al., 1993), the YBT could have been active after ~35 Ma and prior to ~5 Ma ago.

3.2 Topography of the southeastern Tibet margin

A topographic swath across the Jianchuan basin, the YTB and the CHT shows a marked decrease in elevation from west to east, with two steps broadly coinciding with the Yulong (from ~3.5 km to ~2.7 km a.s.l.) and Chenghai (from ~2.7 km to ~1.6 km a.s.l.) thrust belts (Figure 1B). West of the first topographic step, in the hanging wall of the YTB, an area with a mean elevation of ~3.5 km encompasses most of the Jianchuan basin. The present-day landscape is characterized by relict low-relief surfaces as defined by Clark et al. (2006) and Liu-Zeng et al. (2018), but is locally controlled by a set of normal faults bounding the Pliocene-Quaternary Dianwei and Heqing basins (Figures 2, 3, 4G, 4H and 4I). Between the YTB and the CHT-JQTB, the mean elevation is ~2.7 km and the landscape is shaped by incision of the Jinsha River and normal faults bounding the Chenghai Lake. The mean elevation increases gradually to the east close to the CHT-JQTB, which defines a prominent topographic step from ~2.7 km to ~1.6 km, suggesting significant control of thrusting on relief production. In the footwall of the CHT-JQTB, the topography decreases gradually to ~1.6 km (Figure 1B).

4 Methodology and sampling

Apatite fission track (AFT) and apatite (U-Th)/He (AHe) are the two main low-temperature thermochronometres that allow placing constraints on thermal histories of upper crustal rocks related to faulting and/or erosion (Ehlers, 2005; Reiners and Brandon, 2006). They are sensitive to cooling at crustal levels of between 1 to 5 km depth, corresponding to their closure temperatures ranging from 40 to ~120 °C, depending on holding time and composition (Reiners and Brandon, 2006). To constrain the timing and rate of Jianchuan basin exhumation, we collected thirteen samples from Late Eocene syenitic plutons, two from Proterozoic gneiss and one from Eocene sandstone along two elevation transects (i.e., Laonjun Shan and Shamao Shan; Figures 2 and 5; Table 1) for AFT analysis. AHe dating for the Laojun Shan has been reported by Shen et al. (2016); we included these data in our inverse modeling. Two samples from the Shamao Shan were analyzed for AHe (Table 1). Apatite crystals were concentrated using standard mineral separation procedures, including crushing, sieving, magnetic and heavy-liquid separation.

4.1 AFT

AFT analyses were accomplished at Apatite to Zircon, Inc., Viola, Idaho, USA. All samples were analyzed using the LA-ICP-MS approach to determine U-content. The procedures and methods for sample preparation are outlined in Donelick et al. (2005).

Apatite aliquots were mounted in epoxy and polished, and then etched in a 5.5 M HNO_3 solution at 21 °C for 20 s. U contents were acquired using a New Wave Neodymium-YAG 213 nm laser ablation system coupled to a Finigan Element II Magnetic Sector ICP-MS at a 12 μm spot and a 5 Hz repetition rate with the laser set in constant energy mode. Analyses were corrected by ^{43}Ca as an internal standard for variations in ablation volume.

4.2 AHe

AHe analyses were performed at the University of Arizona, USA. Typically, 3-5 clear, intact and euhedral apatite crystals were selected. The dimension of each grain was measured and photographed. Only grains larger than 60 μm in both length and width were accepted for (U-Th)/He analysis. The apatite grains were wrapped into Nb foil tubes and degassed by laser heating, and then analyzed for He using ^{3}He isotope dilution, cryogenic purification and quadrupole mass spectrometry. The U, Th and Sm concentrations of each dissolved aliquot were subsequently measured on a sector inductively coupled plasma-mass spectrometer. (U-Th)/He ages were corrected for α-ejection using the equations from Farley (2002). Standard Fish Canyon Tuff zircon and Durango apatite fragments were analyzed together with unknowns to validate age determinations, age reproducibility and measurement accuracy.

4.3 Thermal modeling

The thermal histories of the Laojun Shan and Shamao Shan samples were modeled using the QTQt inverse modeling code (Gallagher, 2012), which allows inferring thermal histories from multiple samples including different thermochronologic systems collected along age-elevation profiles. We built two sets of models for comparison between different input data sets. The first set only includes AFT ages, track length distributions and kinetic parameters. The second set considers not only the AFT data but also acceptable single-grain AHe ages, apatite crystal dimensions and U, Th and Sm concentrations (Table 3). Fission-track annealing and He diffusion algorithms used for the inverse modeling are from Ketcham et al. (2007) and Gautheron et al. (2009), respectively.

For the first set of models, we imposed two time-temperature constraints. An initial constraint at a temperature of 750±50 °C was set up at 35±2 Ma, based on the emplacement ages of the plutons ranging from 33 to 37 Ma (Gourbet et al., 2017; Lu et al., 2012). A second constraint at a temperature of 90±30 °C was set up at 30±3 Ma based on two considerations: first, the rapid thermal equilibration of igneous rocks emplaced at shallow crustal level (<200 °C) (Annen, 2011); second, the existence of an AFT PAZ as inferred from the age-elevation relationship in the Laojun Shan profile (see below). For the second set of models, we also fixed two time-temperature constraints. The first constraint is similar to that of the first set of models, while the second constraint was extended to 30±5 Ma and 90±50 °C in order to cover the closure temperatures of both the AFT (120-60°C) and AHe (80-40°C) systems, resulting in a wider range of possible cooling histories.

5. Results and interpretation

5.1 AFT

All samples yielded grains that could be satisfactorily analyzed (Table 2). AFT ages range from 18±5 to 37±4 Ma in the Laojun Shan, and from 21±3 to 35±5 Ma in the Shamao Shan. All ages pass the χ^2 test with very low dispersion values, suggesting single age populations (Galbraith and Green, 1990). Mean track lengths range from 13.8 to 15.1 μm, and show little variation (Figures 5A and 5B; Table 2).

The Laojun Shan transect includes two groups of samples (Figure 3). One group (JC22 to JC29) was collected along a ~10-km-distance elevation profile downward the Laojun Shan. The other group (JC30 to JC33) was collected near the village of Shuhe, ~15 km to the north. The sampled intrusive rocks have a similar age and facies (Lu et al., 2012), suggesting a similar origin and emplacement depth. The plutons intrude unmetamorphosed sediments and show a narrow zone with hypovolcanic textures at their margin, indicative of shallow emplacement. There is little evidence for faulting between the Laojun Shan and the Shuhe area (Figures 2b and 3). Eocene sediments of the Jianchuan basin are folded at the contact with magma intrusions and are affected by N-S folds (Gourbet et al., 2017). However, the Late Eocene Jianchuan Fm. (E_2jc), which comprises the youngest strata in the basin and was deposited synchronous to the emplacement of the plutonic rocks, dips monotonically by 15 to 20° to the east (Gourbet et al., 2017). This implies that there was negligible N-S tilting after ~35 Ma between the Laojun Shan and Shuhe transects. This is corroborated by samples JC31 (Shuhe) and JC29 (Laojun Shan), which are located at similar elevations but ~20 km apart, and have similar AFT cooling ages (Figures 3 and 5A). This similarity suggests little variation in exhumation depth and geothermal gradient between the two locations. We therefore integrated the two groups of samples in a single age-elevation transect (Figure 5A).

This integrated transect has ten samples spanning ~1800 m of elevation (Figures 3 and 5A). The four highest samples (JC22, JC23, JC24 and JC26, between 3500 and 4100 m elevation) yield pooled AFT ages between 37.4±4.1 Ma and 31.4±3.1 Ma, overlapping within error the magma intrusive ages of 35.4±0.2 Ma and 35.3±0.4 Ma, as dated by zircon U-Pb geochronology (Gourbet et al., 2017; Lu et al., 2012; Figure 2). These are interpreted to record rapid cooling following pluton emplacement at shallow depth. At elevations between 3500 and 2850 m, AFT ages between 33.1±3.4 and 20.3±2.4 Ma show a positive correlation between age and elevation with a slope of ~0.05±0.02 km/Myr (Figure 5A; Tables 1 and 2). Mean track lengths (13.8-14.6 μm) are relatively long, with standard deviations of 1.1-1.3 μm (Figure 5A; Table 2). , A distinct break in the slope of the age-elevation relationship, anchored by sample JC29, occurs at an elevation of 2850 m. Below that elevation, AFT ages of 21.3±4.4 to 18.0±5.3 Ma define a steep age-elevation trend, but fail to yield a well-constrained apparent exhumation rate due to large errors (Figure 5A; Table 2). These samples should be fully reset based on their long AFT track lengths, and narrow, unimodal distribution pattern, which are consistent with rapid cooling rates (Fitzgerald et al., 1995; Gleadow et al., 1983). The prominent break in age-elevation slope at ~20±5 Ma in the Laojun Shan AFT data thus suggests the onset of exhumation of a fossil AFT PAZ at that age.

The Shamao Shan transect has six samples (CD114 to CD118 & CD193) spanning a limited elevation range between 2276 and 2610 m (Figures 2, 3 and 5B; Table 2). Crystallization of the Shamao Shan pluton is dated between 35.0±0.1 Ma (Schärer et al., 1994) and 35.6±0.3 Ma (Lu et al., 2012). Initial cooling was probably rapid, as a nearby dyke yields an $^{40}Ar/^{39}Ar$ phlogopite age of 35.5±1 Ma, corresponding to a closure temperature of ~450±50°C (Gourbet et al., 2017). Similar to the Laojun Shan pluton, the Shamao Shan pluton was emplaced at shallow depth, but these two plutons are separated by a series of normal faults (Figures 2 and 3; Gourbet et al., 2017).

Sample CD115, from an elevation of 2460 m, has an AFT age of 34.9±4.6 Ma. This age overlaps the pluton emplacement age and probably records rapid cooling following emplacement at shallow depth. The other AFT ages range between 32.5 and 21.0 Ma, and exhibit a gentle age-elevation trend with a slope of ~0.03±0.02 km/Myr (Figure

5B; Table 2). These samples have similar track-length distributions to those in the upper part of the Laojun Shan transect, and thus are interpreted identically. The lowest sample (CD118, 2276 m) has an age of 21.0±3.2 Ma, close to that of the Laojun Shan profile at a comparable height (sample JC30). The lack of samples below 2276 m does not allow detecting if a break in slope exists in the Shamao Shan transect, but a comparison of the elevation of the interpreted PAZ between the two transects suggests ⩾600 m of differential uplift between them after ~20 Ma. This could be caused by a component of down-to-the-east movement along normal faults that are parallel to the Jianchuan fault in between these two profiles (Figures 2 and 3).

5.2 AHe

Single-grain AHe ages were obtained from samples CD114 and CD116 in the Shamao Shan profile (Table 3). Sample CD114 yielded three discordant single-grain ages between 34.0±0.4 Ma and 43.4±0.6 Ma. These ages were rejected because they are much older than the corresponding AFT age of 28.8±4.6 Ma, and two of them are older than the intrusive age of the Laojun Shan pluton (35.6±0.3 Ma; Lu et al., 2012). The lower-elevation sample CD116 yielded three single-grain ages between 26.2±0.3 Ma and 33.5±0.4 Ma (Figure 5B) as well as an outlier at 91.0±0.9 Ma. The 33.5±0.4 Ma age overlaps the crystallization age of the Shamao Shan pluton and may represent rapid cooling during shallow emplacement of the pluton. The other ages overlap nearby AFT ages of samples CD114 and CD117, and record post-intrusion exhumation of the pluton.

5.3 Thermal modeling

Based on (U-Th)/He data sampled along the same elevation transect from the Laojun Shan (Figure 2), Shen et al. (2016) inferred an exhumation episode between 30 and 20 Ma with rates of ~0.10-0.18 km/Myr. However, most of these data yield scattered ages, with several grain ages older than the timing of magma intrusion (Figure 5A). Excluding these ages >35 Ma, the other single-grain ages of Shen et al. (2016) are somewhat younger than our AFT ages at a comparable elevation for high-elevation samples (>3500 m) and overlap with them at lower elevations (Figure 5A). This relationship suggests rapid cooling around 20-30 Ma (e.g., Murray et al., 2016), while the scatter in single-grain AHe ages could be due to variable eU content and/or zoning of the grains (Shen et al., 2016).

Modeling results using QTQt (Gallagher, 2012) are presented in Figure 6A-E for AFT data only, and Figure 6E-H for combined AFT and AHe data, allowing assessment of the impact of including the AHe data in the thermal history models. The first set of models, which do not take the AHe data into account, predict best-fit cooling curves for the Laojun Shan profile that show a four-stage cooling history (Figure 6A-B). Initial rapid cooling between 35-30 Ma (~100 °C/Myr) reflects thermal equilibration for a pluton emplaced at shallow crustal levels (<200 °C). Simple conductive cooling calculations suggest that a pluton emplaced at depths between 5 and 10 km should thermally equilibrate within <1 to ~4 Myr (Braun et al., 2006). This is supported by the fact that AFT ages of high-elevation samples overlap with pluton-emplacement ages of ~35 Ma (Figure 5A). Subsequently, the rocks stayed at temperatures ~100 °C for ~5 Myr. We interpret the following rapid cooling between ~24 and ~20 Ma at a rate of ~20 °C/Myr to record rapid exhumation of the rocks, followed by a protracted period of extremely slow cooling at a rate of <1 °C/Myr (Figure 6A). The predicted AFT ages and mean track lengths (MTL) fit the observed data (Figure 6B). The predicted ages show a positive correlation with elevation, but do not clearly show the break-in-slope inferred from the AFT data (Figure 6B).

In contrast, modeling results for the Shamao Shan present a three-stage cooling history (Figure 6C). A first stage of cooling between 35 and 28 Ma is interpreted to result from thermal equilibration after pluton emplacement, as for the Laojun Shan. The rocks subsequently experienced cooling between ~28 and ~24 Ma at a rate of ~20 °C/Myr. The last episode shows extremely slow cooling at a rate of <1 °C/Myr since ~25 Ma, similar to the Laojun Shan results. The predicted ages and MTL calculated for these cooling histories reproduce the AFT data reasonably well, even though the predicted age-elevation gradient is steeper than the observed one (Figure 6D).

The models taking into account selected AHe data predict best-fit cooling paths for the Laojun Shan that suggest a three-phase thermal history (Figure 6E). A first stage of cooling between 35-27 Ma (~90 °C/Myr) reflects the same process of thermal equilibration of the Laojun Shan pluton as in the first set of models (Figure 6A). The second cooling stage, during ~27-22 Ma at a rate of ~24 °C/Myr, is interpreted to result from rapid exhumation of the rocks, which were brought to near-surface temperatures at ~22 Ma. At that time, the cooling rate decreased dramatically to <0.5 °C/Myr. Modeling results for the Shamao Shan pluton (Figure 6G) present similar cooling histories to the first set of models, but rapid cooling related to rock exhumation is restricted to a very short time span from ~29 to ~26 Ma, at a rate of ~20 °C/Myr. The best-fit models including AHe data reproduce the AFT data equally well as those without, and predict single-grain AHe that lie within the wide range of observed ages (Figures 6F and 6H).

In summary, both sets of inverse models show a first-stage of very rapid cooling (>90 °C/Myr) during 35-30 Ma and 35-28 Ma, which we interpret as recording thermal equilibration of the Laojun Shan and Shamao Shan plutons, respectively, followed by rapid exhumational cooling between ~28-20 Ma and residence at surface temperatures since then. The main difference between the AFT-only models and the models including AHe data is the timing of the rapid exhumation phase, which takes place somewhat later (~24-20 Ma and ~28-24 Ma in the Laojun Shan and Shamao Shan, respectively) for the AFT-only models than in the models including AHe data (~27-22 and ~29-26 Ma in the Laojun Shan and Shamao Shan, respectively). However, all models consistently predict ~4 Myr of rapid Late Oligocene-Early Miocene cooling for both the Laojun Shan and Shamao Shan, at rates of ~20 °C/Myr. Considering reasonable geothermal values (30±5 °C/km), this corresponds to exhumation rates of ~0.57-0.80 km/Myr or ~2.3-3.2 km of total exhumation during this time. Both profiles show exhumation rates lower than ~0.01 km/Myr since ~20 Ma, suggesting less than 0.2 km of exhumation of the Jianchuan basin since the Early Miocene. Rapid Late Oligocene-Early Miocene basin exhumation is consistent with the absence of coeval sedimentation within the basin, as recently evidenced by Gourbet et al. (2017).

6 Discussion

6.1 Mechanisms for rapid exhumation of the Jianchuan basin

It has been hypothesized that the remnant landscapes of southeastern Tibet correspond to an erosion surface formed close to sea level that has been passively uplifted by lower-crustal flow originating from the over-thickened crust of central Tibet (e.g., Clark et al., 2005b; Royden et al., 1997). The timing of uplift is assumed to correspond to a phase of accelerated incision of the main rivers that are entrenched in the plateau. It was inferred that exhumation related to incision started between ~13 and 9 Ma based on low-temperature thermochronology data (Clark et al., 2005a; Ouimet et al., 2010). However, other studies suggest that Miocene exhumation related to river incision started earlier at ~18-9 Ma (McPhillips et al., 2015) or ~22-15 Ma (Tian et al., 2014). In addition, more local Late-Miocene exhumation events are associated with faulting, as for instance the initiation of the left-lateral transtensive Litang fault system at ~6 Ma (Zhang et al., 2015), and that of the Xianshuihe fault at ~9 Ma in the Gongga Shan (Zhang et al., 2017).

Our thermochronological data and modeling results suggest ~2.3 to 3.2 km of exhumation of the Eocene Jianchuan basin in the Late Oligocene-Early Miocene (between ~28 and ~20 Ma). A key question is to decipher the mechanism(s) that drove basin exhumation. The Jianchuan basin is bounded to the west by the Qiaohou thrust belt (Figure 2A). These thrusts dip to the west and the Jianchuan basin is located in their footwall; movement along these thrusts would thus have induced subsidence and burial of the basin rather than exhumation. Bounding the basin to the east, the Jianchuan fault shows normal motion with a possible left-lateral component, that could have induced exhumation of the basin. However, this normal fault is linked to the Lijiang pull-apart zone that initiated probably at ~5 Ma (Leloup et al., 1993), and in any case after the end of left-lateral shear along the ASRR at ~17 Ma (Leloup et al., 2001), incompatible with the ~28-20 Ma cooling/exhumation episode. Within the basin, several faults trends parallel to the Jianchuan fault (Figure 3) and show both strike-slip and normal sense of shear (Figure 4G). Mapping of the faults shows that most of them dip steeply to the ESE and cause downward motion of the eastern compartments (Figures 2D, 2E, 3 and 4G; Gourbet et al., 2017). Taking the limestone of the Jiuziyan Fm. (E_2jz) as a reference bed, we estimated the amount of vertical throw at 400 to 840 m (3120/2680 m-2280 m). These values are broadly consistent with the ⩾600 m vertical throw estimated from the offset of the fossil PAZ between the Laojun Shan and Shamao Shan. We interpret this as an evidence for a normal component of motion along NNE-SSW-striking and east-dipping faults in the eastern Jianchuan basin after 20 Ma, in good accordance with the hypothesis that the Jianchuan fault could be younger than 17 Ma and likely ~5 Ma. The offset of the Jianchuan bounding fault is not known, but appears too small (⩽3 km) to have brought to the surface in its footwall the post-20 Ma AFT PAZ. The Qiaohou and Jianchuan faults now bounding the basin thus do not appear responsible for Late Oligocene-Early Miocene exhumation of the Jianchuan basin.

Alternatively, Shen et al. (2016) proposed that Late Oligocene-Early Miocene basin exhumation, at a relatively slow rate of ~0.10-0.18 km/Myr as inferred from their AHe data, was linked to river incision related either to early lower-crustal flow or to transpressional deformation in southeastern Tibet. However, these authors did not elucidate how the river incision was genetically linked with evolution of local rivers (e.g., Jinsha River) and which transpressional structure(s) could account for the exhumation. Whether the ancient Jinsha River flowed through the Jianchuan basin is largely disputed (e.g., Clark et al., 2004; Wei et al., 2016; Wissink et al., 2016). Eocene fluvial sediments of the Baoxiangsi Fm. (E_2b; Figure 2) indicate that a large braided river flowed through the Jianchuan basin before ~36 Ma (Gourbet et al., 2017) but this predates basin exhumation by more than 10 Ma. Recent cosmogenic nuclide studies on cave sediments near the first bend of the modern Jinsha River (Figure 2) suggest ~1 km river incision during 18-9 Ma (McPhillips et al., 2015), thus postdating Jianchuan basin exhumation. Our new data show that major exhumation of the Jianchuan basin took place during the Late Oligocene-Early Miocene, with extremely low exhumation of <0.2 km since then ruling out southward flow of a large river across the basin in the Neogene. Therefore, neither the paleo (⩾35 Ma) nor modern (⩽20 Ma) Jinsha river may have been responsible for the Late Oligocene-Early Miocene (~28-20 Ma) exhumation of the Jianchuan basin. In contrast, the timing of river diversion is broadly compatible with exhumation of the basin and could be genetically related to it.

Another possibility is that thrusting of the N-trending, W-dipping YTB may have triggered exhumation of the Jianchuan basin. Crosscutting relationships indicate that thrusting took place between ~35 Ma and ~5 Ma. The timing of folding of the Yulong anticline, estimated at 17±3.5 Ma (Lacassin et al., 1996), is roughly compatible with the age of the YTB. This age encompasses within uncertainties that of rapid exhumation of the Jianchuan basin. Therefore, we argue that exhumation of the Jianchuan basin was probably related to thrusting along the YTB. Associated folding and uplift in the YTB and Yulong anticline could have been responsible for diversion of the Jinsha River to its modern course, consistent with a major change in composition of Red River-derived sediments in the Hanoi basin ≥24 Ma (Clift et al., 2006).

Based on their morphologic analysis, Liu-Zeng et al. (2008) proposed that the steep topographic step of ~1.8-2.4 km between the Yunnan highlands and southeastern Tibet (Figure 1) was possibly linked to Cenozoic thrusting. AFT ages of ~27-100 Ma with relatively short track lengths (Wilson and Fowler, 2011; Figure 1) suggest that rocks in the hanging wall of these thrusts (i.e., YTB and CHT) have been less exhumed than those in the footwall, as for example in the Jianchuan basin. Our estimate of ~2.3-3.2 km of Late Oligocene-Early Miocene rapid rock exhumation in the hanging wall of the YTB would broadly correspond to the present-day ~1.8-2.4 km of topographic step across the YTB and CHT-JQTB, notwithstanding that the topography has later been disturbed by normal faulting that locally created Pliocene-Quaternary basins (Figures 1B and 3). Such an amount of basin exhumation is roughly compatible with the magnitude of Oligocene-Miocene shortening and rock uplift across the YTB and CHT-JQTB (Clark et al., 2004; Perrineau, 2010).

However, our evidence for Late Oligocene-Early Miocene rapid exhumation of the Jianchuan basin does not exclude the possibility that substantial crustal thickening and corresponding elevation gain in southeastern Tibet occurred prior to the Oligocene or even the India-Asian collision. For example, Lacassin et al. (1996) documented an early phase of deformation in the Yulong anticline at ~36 Ma, which they interpreted as a phase of crustal thickening predating initiation of left-lateral shear along the ASRR.

Tapponnier et al. (2001) interpreted significant Eocene thickening of southeastern Tibet as a first stage of building of the Tibetan plateau. Recently, a multiple-thermochronometer study revealed two periods of rapid rock exhumation during the Middle to Late Cretaceous and Early Cenozoic for the low-relief areas in southeastern Tibet (Liu-Zeng et al., 2018). These two exhumation events are broadly consistent with rapid exhumation in central Tibet between 85-45 Ma (Rohrmann et al., 2012) and probably resulted from significant crustal shortening during the collision between the Lhasa and Qiangtang terranes (e.g., Kapp et al., 2005, 2007). Such early thickening could have triggered moderate surface uplift recorded by paleoaltimetry analyses (Hoke et al., 2014; Li et al., 2015; Tang et al., 2017) and erosion of parts of the eastern and southern Tibetan plateau, clasts from which were deposited in Eocene basins such as the Jianchuan basin. Our data only document exhumation of the Jianchuan basin after basin infilling, and thus neither confirm nor preclude the existence of Cretaceous to Eocene crustal shortening that could have partly shaped the landscape of the margins of southeastern Tibet.

6.2 Regional tectonic implications

Exhumation of the Jianchuan basin at ~28-20 Ma is broadly coeval with other exhumation events around the southeastern Tibet (Figure 1A), suggesting a regional cause for exhumation. The Longmen Shan thrust belt could have extended southward, merging with the YTB prior to offset by the Xianshuihe fault (Burchfiel et al., 1995;

Wang et al., 1998; Yan and Lin, 2015). In this case, upper crustal shortening and thickening probably affected a large area from the Longmen Shan to the Laojun Shan in the Oligocene-Early Miocene (Figure 1A), and would be responsible for the generation of similar topographic relief above major thrust faults along the margins of southeastern Tibet. However, Oligocene-Miocene sediments are pervasively absent in the footwalls of the Yalong-Yulong and Longmen Shan thrust belts (BGMRY, 1990; Deng et al., 2017). This is also the case for some large basins in southeastern Tibet, as for instance the Sichuan, Xichang and Chuxiong basins (Deng et al., 2017; Figure 1A). One possible explanation is that southeastern Tibet was not a closed system for water and sediments (Richardson et al., 2008); large amounts of eroded sediments may have been transferred by large rivers and eventually deposited into the peripheral seas. Rapid exhumation in the hanging walls of the thrusts led to accelerating surface erosion and ultimately may have contributed significantly to the peak in sediment fluxes observed in southeast Asia seas during Oligocene-Miocene times (Clift, 2006).

At a regional scale, Late Oligocene-Early Miocene crustal shortening and thickening coincides with strong left-lateral shearing along the ASRR (Leloup et al., 2001), as well as with activity of the Jiali (Lee et al., 2003; Lin et al., 2009) and Chongshan (Zhang et al., 2012) shear zones. These kinematics indicate SE-NW regional compression related to convergence between the northwest corner of the India plate and the Asian plate at this time. The end of this episode of crustal shortening generally predated the onset of the left-lateral Kunlun strike-slip fault (Duvall et al., 2013; Jolivet et al., 2003), Ganzi-Xianshuihe-Xiaojiang fault (Wang et al., 2009; Zhang et al., 2017), Litang fault (Zhang et al., 2015) and dextral strike slip of the Gaoligong fault (Lin et al., 2009; Zhang et al., 2010). Overall, the synchronicity of major crustal deformations favours a Late Oligocene-Early Miocene tectonic configuration in which a southward extruded block was bounded by the Jiali fault-ASRR to the southeast (e.g., Lin et al., 2009; Zhang et al., 2010), with the YTB, Chenghai, Muli, Jinghe-Qinghe and Longmen Shan thrust belts further north that created topographic relief on the margins of southeastern Tibet (Figure 7).

7 Conclusions

In order to unravel the timing and mechanisms of uplift of southeastern Tibet, this study presents structural and morphological analyses of the YTB, and reconstructs the cooling and exhumation history of the Jianchuan basin through thermal modeling of AFT and AHe thermochronology data. Structural analysis along the YTB provides evidence for post-Eocene thrusting, coincident with a present-day topographic step of 1.8-2.4 km detected by morphometric analysis. AFT and AHe thermochronology assisted by thermal modeling reveals 2.3-3.2 km of rapid exhumation in the Jianchuan basin in the hanging wall of the YTB in the Late Oligocene-Early Miocene (~28-20 Ma) at a rate of ~0.57-0.80 km/Myr. Exhumation of the Jianchuan basin since ~20 Ma is limited to <0.2 km. These results suggest that activity of the YTB occurred during the Late

Oligocene-Early Miocene, synchronous with and related to thrusting in the Longmen Shan, and that drainage rearrangement and topographic relief development on the margins of southeastern Tibet could have been mostly generated by thrusting at that time.

Acknowledgements

We thank Ganqing Xu, Yuntao Tian, Marie-Luce Chevalier, Paul O'Sullivan and Paul Kapp for enlightening discussions, and Kerry Gallagher for offering us updated QTQt software and constructive suggestions on modeling issues. We are grateful to Peter Reiners and Uttam Chowdhury for access to the (U-Th)/He lab at the University of Arizona. We also thank three anonymous reviewers for helpful comments that improved the manuscript and editor Nathan Niemi for editorial handling. This study was funded the National Science Foundation of China (Nos. 41672195, 91755213, 41202144, 41302279), the Geological Survey of China (No. 1212011121261), the Fundamental Research Funds for the Central Universities, China University of Geosciences (No. G1323511641), China Scholarship Council (No. 201606415003) and Ministry of Natural Resources (No. cdcgs2018001). This project was supported by the Cai Yuanpei program (27968UC) of the China Scholarship Council/French Ministry of Education, and the SYSTER (Institut National des Sciences de l'Univers du CNRS) program. All the data used are listed in the references or archived in Figshare repository (https://figshare.com/s/69ecce70ba9a99443b22).

Table 1. Sample information in the Jianchuan basin, western Yunnan.

Sample	Lithology	Era	Longitude (°E)	Latitude (°N)	Elevation (m)	Dating method
JC22	Syenite	35.4 ± 0.3 Ma[a]	99.7043	26.6302	4045	AFT
JC23	Syenite	35.4 ± 0.3 Ma[a]	99.7128	26.6320	3953	AFT
JC24	Syenite	35.4 ± 0.3 Ma[a]	99.7302	26.6433	3832	AFT
JC26	Sandstone	Eocene	99.7683	26.6451	3491	AFT
JC27	Porphyry	35.4 ± 0.3 Ma[a]	99.7807	26.6607	3317	AFT
JC28	Porphyry	35.4 ± 0.3 Ma[a]	99.8009	26.6595	3058	AFT
JC29	Porphyry	35.4 ± 0.3 Ma[a]	99.8150	26.6561	2848	AFT
JC30	Porphyry	35.7 ± 0.2 Ma[a]	99.7718	26.7779	2130	AFT
JC31	Gneiss	Proterozoic	99.8125	26.8224	2724	AFT
JC33	Gneiss	Proterozoic	99.8153	26.7891	2019	AFT
CD114	Porphyry	35.6 ± 0.3 Ma[a]	99.9087	26.5874	2531	AFT, AHe
CD115	Porphyry	35.6 ± 0.3 Ma[a]	99.9100	26.5877	2460	AFT
CD116	Porphyry	35.6 ± 0.3 Ma[a]	99.9111	26.5883	2394	AHe
CD117	Porphyry	35.6 ± 0.3 Ma[a]	99.9115	26.5887	2342	AFT
CD118	Porphyry	35.6 ± 0.3 Ma[a]	99.9132	26.5891	2276	AFT
CD193	Porphyry	35.6 ± 0.3 Ma[a]	99.9069	26.5844	2610	AFT

[a] SHRIMP zircon U-Pb age for magma intrusion from Lu et al. (2012).

Table 2. Apatite fission-track results in the Jianchuan basin, western Yunnan.

		Spontaneous tracks						Length, D_{par} and D_{per}			
Sample	N_{g}[a]	No.	Density (10^{5} cm^{-2})	U[b] (ppm)	$P(\chi^{2})$[c] (%)	Dispersion (%)	Pooled age[d] ± 1σ (Ma)	Length[e] ± 1σ (μm)	N_{l}[f]	D_{par} (μm)	D_{per} (μm)
Laojun Shan transect											
JC22	38	359	7.93	21.31	55	0.03	37.4 ± 4.1	14.14 ± 1.17	56	2.22	0.43
JC23	40	464	12.21	8.51	100	0.00	31.4 ± 3.1	14.56 ± 1.23	143	2.28	0.44
JC24	40	439	11.22	7.35	42	0.36	32.3 ± 3.3	14.11 ±1.37	164	2.16	0.40
JC26	37	450	11.22	11.12	62	0.00	33.1 ± 3.4	14.14 ± 1.33	150	1.99	0.40
JC27	39	214	6.19	4.72	90	0.00	28.5 ± 4.1	14.23 ± 1.33	131	2.09	0.39
JC28	35	127	4.65	3.99	58	0.01	27.0 ± 5.2	14.19 ± 1.13	151	1.93	0.37
JC29	32	313	12.74	9.45	95	0.00	20.3 ± 2.4	14.17 ± 1.13	162	2.05	0.36
JC30	40	97	3.76	2.66	44	0.25	21.3 ± 4.4	13.97 ± 1.19	101	1.80	0.34
JC31	29	81	3.43	3.11	26	0.56	19.5 ± 4.4	13.83 ± 1.15	153	1.99	0.35
JC33	22	51	2.35	5.91	68	0.00	18.0 ± 5.3	14.00 ± 0.68	19	1.94	0.36
Shamao Shan transect											
CD114	24	165	4.75	6.68	41	0.01	28.8 ± 4.6	14.41 ± 1.07	151	2.04	0.37
CD115	25	258	6.09	6.87	39	0.03	34.9 ± 4.6	14.71 ± 0.94	156	1.95	0.36
CD117	30	226	7.11	10.67	25	0.66	26.2 ± 3.6	14.57 ± 1.63	161	1.98	0.38
CD118	30	187	7.36	10.67	47	0.02	21.0 ± 3.2	14.13 ± 1.27	156	1.96	0.36
CD193	40	411	10.44	6.60	64	0.01	32.5 ± 3.4	15.06 ± 1.04	172	2.28	0.43

[a] Number of grains dated.

[b] Mean uranium content of all crystals measured using LA-ICP-MS.

[c] Probability obtaining Chi-square value for υ degrees of freedom ($\upsilon=N-1$).

[d] Pooled ages of all grains.

[e] Track length measured after ^{252}Cf irradiation, original mean track length.

[f] Number of track length measured.

Table 3. Apatite (U-Th)/He results from the Shamao Shan in the Jianchuan basin, western Yunnan.

Sample	Aliq.	Th/U	Grain mass (μg)	Ejection corr. (F_T238)	Ejection corr. (F_T235)	Ejection corr. (F_T232)	Grain length (μm)	Grain width (μm)	Rs (μm)	4He (ncc)	U (ppm)	Th (ppm)	Sm (ppm)	eU (ppm)	Uncorr. He age (Ma)	F_T-Corr. He age (Ma)	1σ (Ma)
CD114	*a1	18.27	11.02	0.82	0.799	0.799	289.8	159.0	83.4	0.06	4.25	75.73	194.37	22.05	~~34.99~~	~~43.43~~	~~0.55~~
	*a2	10.32	12.55	0.84	0.813	0.813	277.1	176.0	89.6	0.07	6.59	66.32	244.61	22.18	~~32.22~~	~~39.24~~	~~0.45~~
	*a3	6.50	9.40	0.82	0.792	0.792	251.1	156.7	80.1	0.06	12.69	80.47	242.75	31.60	~~27.34~~	~~34.04~~	~~0.37~~
CD116	a1	7.67	15.43	0.84	0.821	0.821	88.6	349.3	94.3	0.12	12.59	94.14	247.85	34.71	27.79	33.46	0.37
	a2	7.21	43.30	0.89	0.873	0.873	349.3	177.2	134.5	0.26	11.69	82.16	379.33	31.00	25.92	29.45	0.31
	a3	7.23	15.68	0.85	0.833	0.833	408.0	265.4	101.3	0.09	11.79	83.08	178.31	31.32	22.02	26.16	0.28
	*a4	5.94	34.16	0.87	0.856	0.856	306.2	200.1	118.2	0.56	12.85	74.43	311.91	30.34	~~78.68~~	~~90.95~~	~~0.94~~

* Ages were deemed outliers and not used for weighted mean age calculation and inverse modeling because they are older than zircon U-Pb ages of sampled igneous rocks.

FIGURE CAPTIONS

Figure 1. (**A)** simplified geology and topography of southeastern Tibet, with major Cenozoic faults, modified from Leloup et al. (1995) and E. Wang et al. (2012). The inset shows location within Asia. Abbreviations: AFT PAZ–Apatite fission-track partial annealing zone, ASRR–Ailao Shan-Red River shear zone, CD–Chuandian block, CHT–Chenghai thrust, CSSZ–Chongshan shear zone, JQTB–Jinhe-Qinghe thrust belt, RRF–Red River fault, YTB–Yulong thrust belt. White stars denote accelerated exhumation phases constrained by thermochronology in southeastern Tibet, with black numbers indicating the duration: 0–This study, 1–E. Wang et al. (2012), 2–Tian et al. (2015), 3–Clark et al.(2005a) and Ouimet et al. (2010), 4–Godard et al. (2009), 5–Xu and Kamp (2000), 6–Zhang et al. (2017), 7–S. Wang et al. (2012), 8–Tian et al. (2014), 9–Zhang et al. (2016), 10–Lacassin et al. (1996), 11–Yang et al. (2017), and 12–Wilson and Fowler (2011). Blue numbers indicate paleoaltimetry estimates: 13–Hoke et al. (2014), 14–Li et al. (2015), 15–Gourbet et al. (2017), 16–Tang et al. (2017). Ages for the onset of major active faults appear in red: 0-YTB (this study), a–western and eastern portions of the Kunlun fault (Duvall et al., 2013; Jolivet et al., 2003), b–Longmen Shan thrust belt, c–Xianshuihe-Xiaojiang (Zhang et al., 2017), d–Ganzi fault (Wang et al., 2009), e–Litang fault (Zhang et al., 2015), f-JQTB (S. Wang et al., 2012). Ages for the duration of major faults appear in red: g-sinistral shear of the RRF during ~34-17 Ma (Leloup et al., 2001) and kinematic reversal at ~10/5-0 Ma (Leloup et al., 1995; Replumaz et al., 2001), h–Jiali fault (Lin et al., 2009),

i–Parlung fault (Lee et al., 2003), j–Gaoligong fault (Lin et al., 2009; Zhang et al., 2012), k–Chongshan shear zone (Zhang et al., 2010). (**B)** morphotectonic cross section superimposed on topographic swath (black dotted box in Figure 1A) generated from 30-m resolution ASTER GDEM across the YTB and CHT-JQTB in western Yunnan. Vertical exaggeration: 10x. Main faults have the same legend as Figure 1A.

Figure 2. (**A)** Simplified geological map of the Lijiang-Jianchuan area based on BGMRY (1990), Gourbet et al. (2017) and our new observations. (**B)** and **(C)** stereo plots (lower hemisphere projection) of brittle faults in the YTB at site CD357, and sites JC46, CD101, CD305 and CD306, respectively. (**D**) and (**E**) Geological cross sections through the YTB and the Jianchuan basin, showing contact relationships between different structural and lithological units and sampling strategies for AFT and AHe. Vertical exaggeration 2.5x.

Figure 3. Geological map of the Jianchuan basin, showing locations of geochronological and thermochronological samples and ages. For lithological and structural legends, see Figure 2.

Figure 4. Representative field photos of brittle deformation in the YTB to the east of the Jianchuan basin. (**A)** thrust fault cutting across Eocene conglomerates at site CD101, with slickensides and striations on fault planes showing right-lateral/reverse

motion (see trend and kinematics in Figure 2B). (**B)** semi-solidified fault breccias and cataclasites within the fault zone at site CD305, within which slickensides and striations indicate thrusting (see trend and kinematics in Figure 2B). (**C**) a series of minor faults within the Yulong thrust displacing Eocene conglomerates and juxtaposing Triassic siltstone and Eocene sediments at site CD357. (**D)** at the same locality CD357, slickensides and striations on the fault planes indicate early thrusting and normal faulting at a later stage. (**E**) Detail of lense-shaped breccias within the fault zone showing reverse motion at site CD357 (see location in Figure 4D). (**F**) Detail of striations and slickensides on the fault plane indicative of normal motion (see location in Figure 4D). (**G**) Fault in the Baoxiangsi Fm. to the northwest of the Shamao Shan pluton, showing slightly oblique striations with a normal apparent motion trending N150°.

Figure 5. AFT and AHe age-elevation relationships in the Jianchuan basin, western Yunnan. AFT and AHe ages are plotted against elevation for the Laojun Shan (**A**) and Shamao Shan (**B**) profiles, respectively. Black symbols represent samples with AFT ages that correspond to post-emplacement pluton cooling, while blue symbols are samples record later exhumation. Age-elevation relationship for this sample is given with corresponding correlation coefficient (R^2). A clear break-in-slope occurs at ~20± 5 Ma in the Laojun Shan profile; red symbols correspond to samples from below the break in slope that suggest very rapid exhumation. Confined track-length distributions

for each sample are shown in the insets. Grey dots correspond to single-grain AHe ages from the Laojun Shan transect reported by Shen et al. (2016); light grey data have not been used in QTQt inversions. Black dots represent AHe data from the Shamao Shan transect from this study used in the QTQt models, while white dots denote AHe data excluded from the models.

Figure 6. Thermal histories of the Jianchuan basin, western Yunnan. Cooling histories of the Laojun Shan and Shamao Shan **are** derived from QTQt inverse modeling based on AFT data (A, **C**) and AFT in combination with AHe data **(E**, **G**). (**B**), (**D**), (**F**) and (H) **show the** fits of the predicted **and** observed data. The thermal history of the uppermost sample is **shown in** blue, with the 95% confidence interval in cyan**,** while the thermal history of the lowermost sample is **shown in** red, with the 95% confidence interval in magenta. Thermal histories for samples **at** intermediate **elevations** are in grey. These reflect the combined uncertainty in the inferred thermal history and the offset parameters.

Figure 7. Late Oligocene-Early Miocene tectonic scenario for southeastern Tibet in the framework of India-Asian convergence, highlighting SE-NW-directed compression leading to a large-scale southeastward-extruded crust block accommodated by the ASRR along the southwest and thrust faults that are responsible for relief generation in the southeastern front (see details in discussion). Abbreviations: ASRR–Ailao Shan-Red River shear zone, CSSZ–Chongshan shear zone, JQTB–Jinhe-Qinghe thrust belt, RRF–Red River fault, YTB–Yulong thrust belt.

Figure 1.

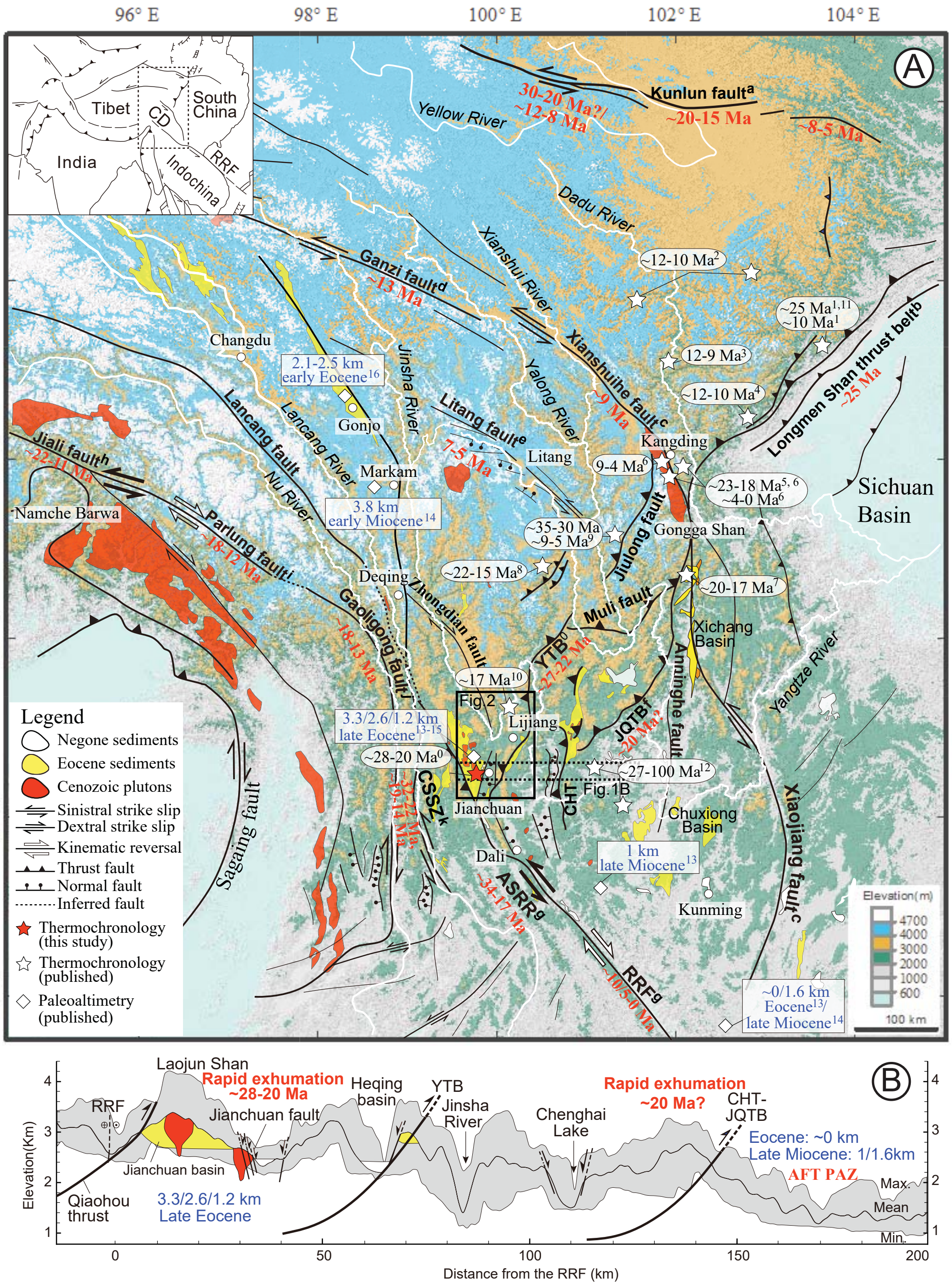96° E
98° E
100° E
102° E
104° E
34° N
32° N
30° N
28° N
26° N
24° N
A
Tibet
South China
India
Indochina
CD
RRF
Kunlun fault[a]
30-20 Ma?/ ~12-8 Ma
~20-15 Ma
~8-5 Ma
Yellow River
Dadu River
Ganzi fault[d]
~13 Ma
Xianshui River
~12-10 Ma[2]
~25 Ma[1,11] ~10 Ma[1]
Longmen Shan thrust belt[b]
~25 Ma
Changdu
2.1-2.5 km early Eocene[16]
Gonjo
Jinsha River
Litang fault[e]
Yalong River
Xianshuihe fault[c]
~9 Ma
12-9 Ma[3]
~12-10 Ma[4]
Kangding
Jiali fault[h]
~22-11 Ma
Lancang fault
Lancang River
Markam
7-5 Ma
Litang
9-4 Ma[6]
~23-18 Ma[5, 6] ~4-0 Ma[6]
Sichuan Basin
Namche Barwa
Parlung fault[i]
~18-12 Ma
Nu River
3.8 km early Miocene[14]
~35-30 Ma ~9-5 Ma[9]
Gongga Shan
Jiulong fault
Deqing
~22-15 Ma[8]
~20-17 Ma[7]
Zhongdian fault
Muli fault
Gaoligong fault[j]
18-13 Ma
YTB
27-22 Ma
Xichang Basin
Anninghe fault
Yangtze River
~17 Ma[10]
Fig.2
Lijiang
JQTB[f]
20 Ma?
3.3/2.6/1.2 km late Eocene[13-15]
~28-20 Ma[0]
~27-100 Ma[12]
Fig.1B
CSSZ[k]
32-22 Ma ~10-14 Ma
CHT
Jianchuan
Chuxiong Basin
Sagaing fault
Dali
1 km late Miocene[13]
ASRR[g]
34-17 Ma
Kunming
Xiaojiang fault[c]
RRF[g]
~10/5-0 Ma
~0/1.6 km Eocene[13]/ late Miocene[14]
Elevation(m)
4700
4000
3000
2000
1000
600
100 km
Legend
Negone sediments
Eocene sediments
Cenozoic plutons
Sinistral strike slip
Dextral strike slip
Kinematic reversal
Thrust fault
Normal fault
Inferred fault
Thermochronology (this study)
Thermochronology (published)
Paleoaltimetry (published)
B
Laojun Shan
Rapid exhumation ~28-20 Ma
RRF
Heqing basin
YTB
Jinsha River
Jianchuan fault
Chenghai Lake
Rapid exhumation ~20 Ma?
CHT-JQTB
Eocene: ~0 km
Late Miocene: 1/1.6km
AFT PAZ
Jianchuan basin
Qiaohou thrust
3.3/2.6/1.2 km Late Eocene
Max.
Mean
Min.
Elevation(Km)
4
3
2
1
0
50
100
150
200
Distance from the RRF (km)

Figure 2.

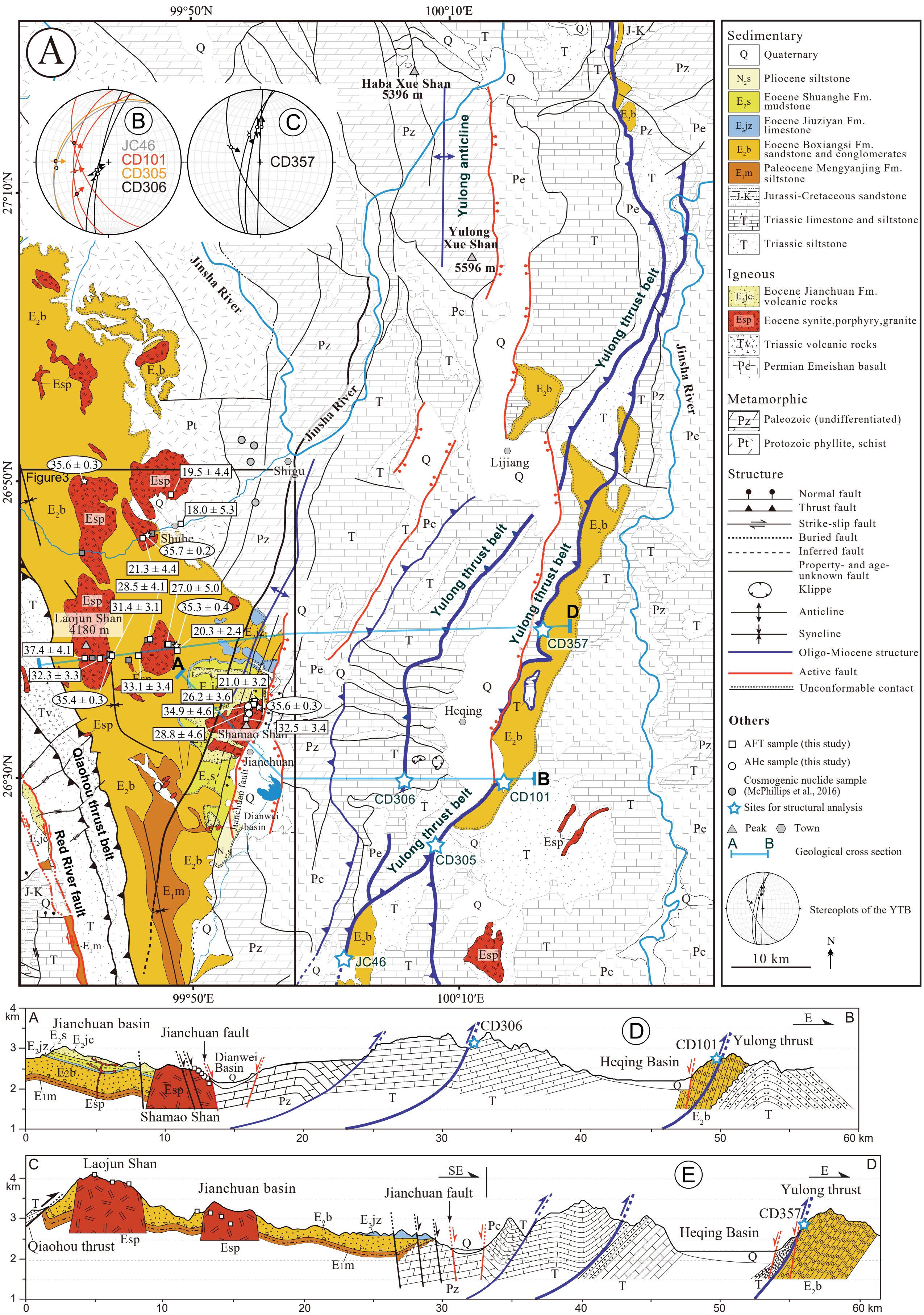

A
B
C
D
E
99°50′N
100°10′E
99°50′E
27°10′N
26°50′N
26°30′N
JC46
CD101
CD305
CD306
CD357
Haba Xue Shan
5396 m
Yulong Xue Shan
5596 m
Yulong anticline
Yulong thrust belt
Jinsha River
Shigu
Lijiang
Heqing
Jianchuan
Jianchuan fault
Dianwei basin
Shuhe
Laojun Shan
4180 m
Shamao Shan
Qiaohou thrust belt
Red River fault
Figure3
35.6 ± 0.3
19.5 ± 4.4
18.0 ± 5.3
35.7 ± 0.2
21.3 ± 4.4
28.5 ± 4.1
27.0 ± 5.0
31.4 ± 3.1
35.3 ± 0.4
20.3 ± 2.4
37.4 ± 4.1
32.3 ± 3.3
33.1 ± 3.4
21.0 ± 3.2
26.2 ± 3.6
35.4 ± 0.3
34.9 ± 4.6
35.6 ± 0.3
28.8 ± 4.6
32.5 ± 3.4
Sedimentary
Q Quaternary
N2s Pliocene siltstone
E2s Eocene Shuanghe Fm. mudstone
E2jz Eocene Jiuziyan Fm. limestone
E2b Eocene Boxiangsi Fm. sandstone and conglomerates
E1m Paleocene Mengyanjing Fm. siltstone
J-K Jurassic-Cretaceous sandstone
T Triassic limestone and siltstone
T Triassic siltstone
Igneous
E2jc Eocene Jianchuan Fm. volcanic rocks
Esp Eocene synite,porphyry,granite
Tv Triassic volcanic rocks
Pe Permian Emeishan basalt
Metamorphic
Pz Paleozoic (undifferentiated)
Pt Protozoic phyllite, schist
Structure
Normal fault
Thrust fault
Strike-slip fault
Buried fault
Inferred fault
Property- and age-unknown fault
Klippe
Anticline
Syncline
Oligo-Miocene structure
Active fault
Unconformable contact
Others
AFT sample (this study)
AHe sample (this study)
Cosmogenic nuclide sample (McPhillips et al., 2016)
Sites for structural analysis
Peak
Town
A B Geological cross section
Stereoplots of the YTB
10 km
N
km
Jianchuan basin
Jianchuan fault
Dianwei Basin
Shamao Shan
Heqing Basin
Yulong thrust
E
SE
Laojun Shan
Qiaohou thrust
0
10
20
30
40
50
60 km
1
2
3
4

Figure 3.

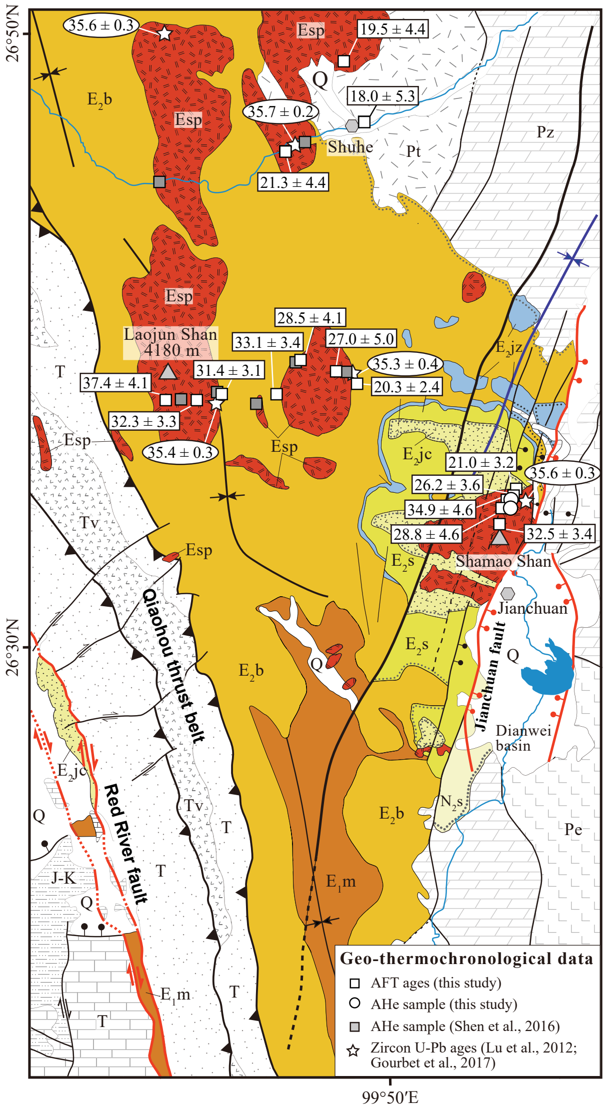
26°50′N
26°30′N
99°50′E
35.6 ± 0.3
Esp
19.5 ± 4.4
Q
E$_2$b
35.7 ± 0.2
18.0 ± 5.3
Pz
Shuhe
Pt
21.3 ± 4.4
Laojun Shan
4180 m
28.5 ± 4.1
33.1 ± 3.4
27.0 ± 5.0
35.3 ± 0.4
20.3 ± 2.4
E$_2$jz
T
37.4 ± 4.1
31.4 ± 3.1
32.3 ± 3.3
35.4 ± 0.3
E$_2$jc
21.0 ± 3.2
35.6 ± 0.3
26.2 ± 3.6
34.9 ± 4.6
28.8 ± 4.6
32.5 ± 3.4
Tv
E$_2$s
Shamao Shan
Jianchuan
Qiaohou thrust belt
Jianchuan fault
Dianwei basin
N$_2$s
Red River fault
J-K
E$_1$m
Pe
Geo-thermochronological data
□ AFT ages (this study)
○ AHe sample (this study)
■ AHe sample (Shen et al., 2016)
☆ Zircon U-Pb ages (Lu et al., 2012; Gourbet et al., 2017)

Figure 4.

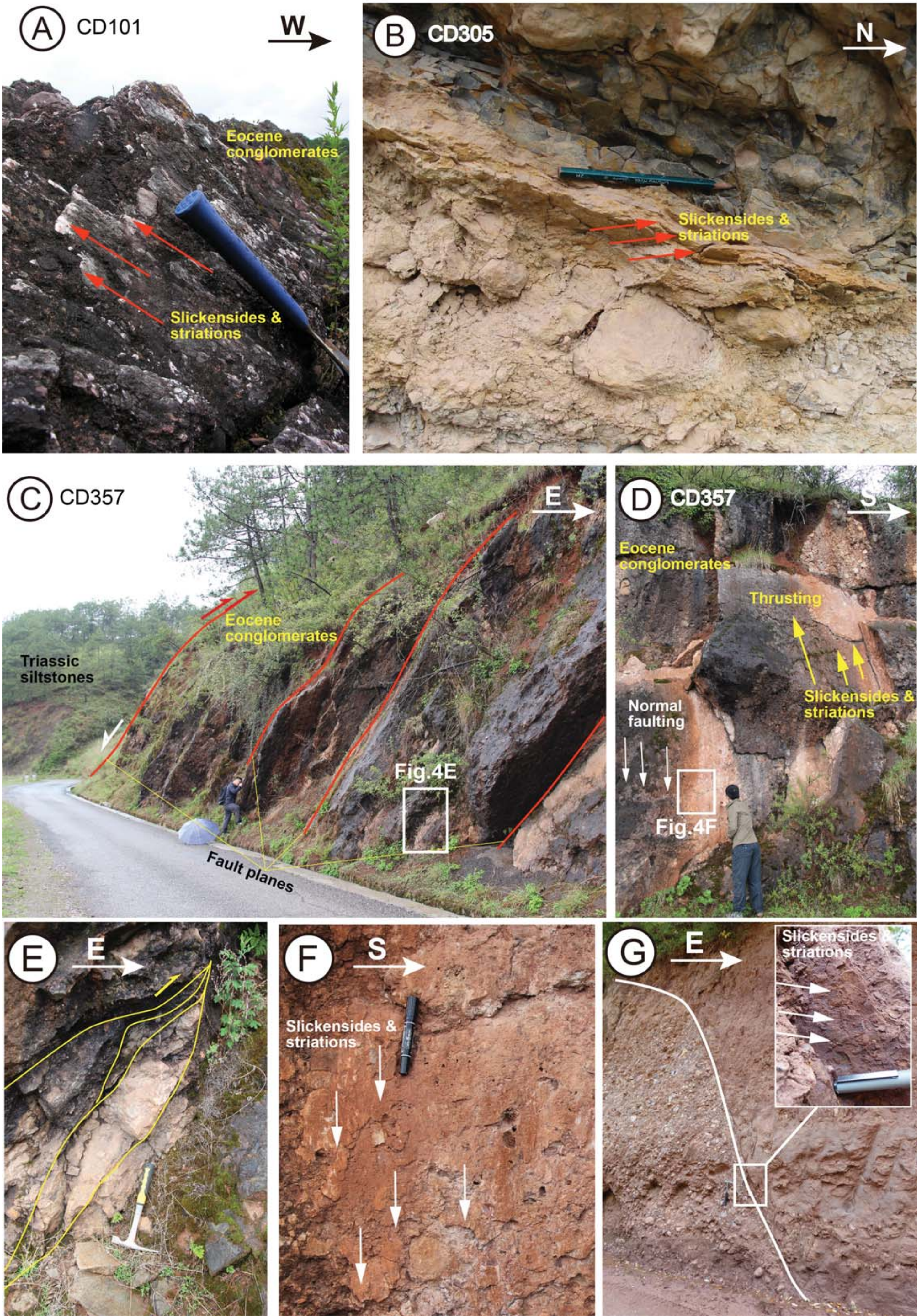
A
CD101
W
Eocene conglomerates
Slickensides & striations
B
CD305
N
Slickensides & striations
C
CD357
E
Eocene conglomerates
Triassic siltstones
Fig.4E
Fault planes
D
CD357
S
Eocene conglomerates
Thrusting
Slickensides & striations
Normal faulting
Fig.4F
E
E
F
S
Slickensides & striations
G
E
Slickensides & striations

Figure 5.

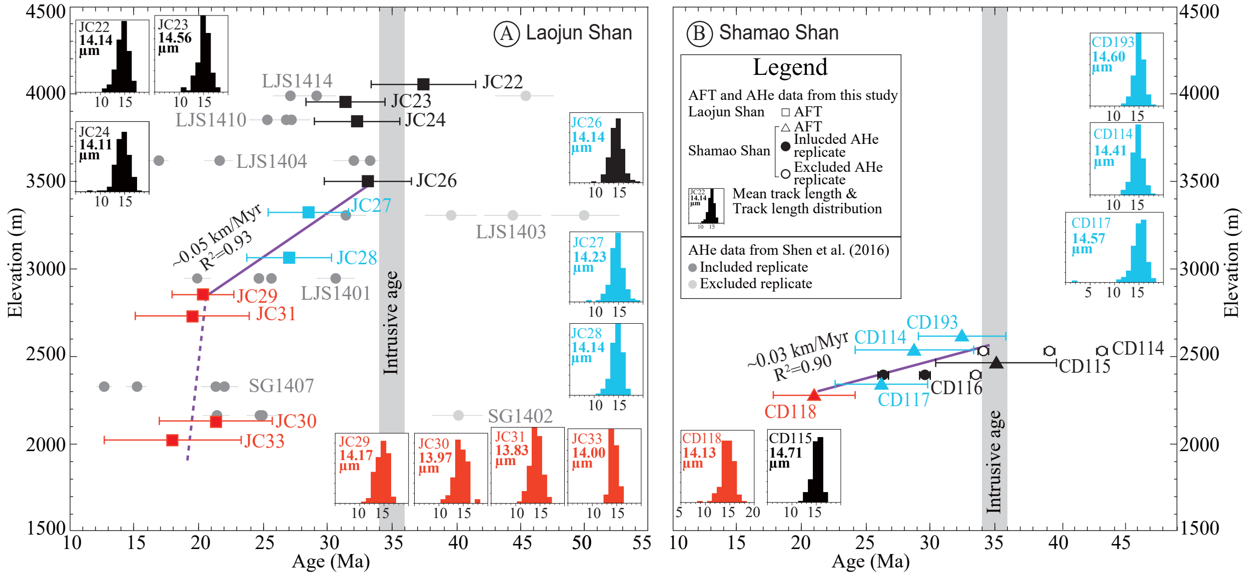
A Laojun Shan
B Shamao Shan
Elevation (m)
Age (Ma)
Intrusive age
~0.05 km/Myr
R²=0.93
~0.03 km/Myr
R²=0.90
JC22
JC23
JC24
JC26
JC27
JC28
JC29
JC31
JC30
JC33
LJS1414
LJS1410
LJS1404
LJS1403
LJS1401
SG1407
SG1402
JC22 14.14 µm
JC23 14.56 µm
JC24 14.11 µm
JC26 14.14 µm
JC27 14.23 µm
JC28 14.14 µm
JC29 14.17 µm
JC30 13.97 µm
JC31 13.83 µm
JC33 14.00 µm
CD193
CD114
CD117
CD118
CD115
CD116
CD193 14.60 µm
CD114 14.41 µm
CD117 14.57 µm
CD118 14.13 µm
CD115 14.71 µm
Legend
AFT and AHe data from this study
Laojun Shan □ AFT
Shamao Shan △ AFT
● Inlucded AHe replicate
○ Excluded AHe replicate
Mean track length & Track length distribution
AHe data from Shen et al. (2016)
● Included replicate
● Excluded replicate
4500
4000
3500
3000
2500
2000
1500
10
15
20
25
30
35
40
45
50
55

Figure 6.

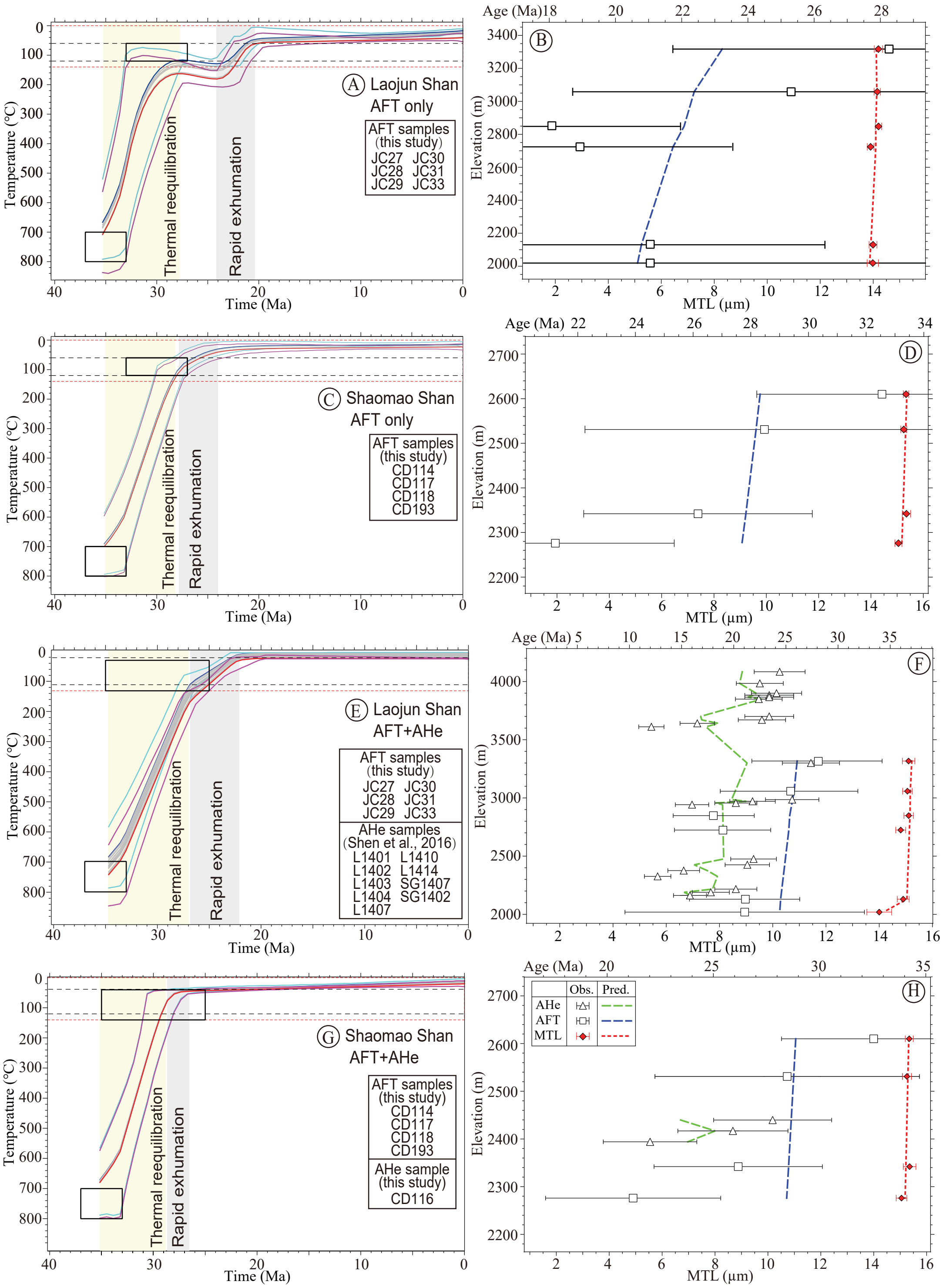
A Laojun Shan
AFT only
AFT samples
(this study)
JC27 JC30
JC28 JC31
JC29 JC33
Thermal reequilibration
Rapid exhumation
Temperature (°C)
0
100
200
300
400
500
600
700
800
40
30
20
10
0
Time (Ma)
Age (Ma) 18
20
22
24
26
28
B
Elevation (m)
3400
3200
3000
2800
2600
2400
2200
2000
2
4
6
8
10
12
14
MTL (µm)
C Shaomao Shan
AFT only
AFT samples
(this study)
CD114
CD117
CD118
CD193
Thermal reequilibration
Rapid exhumation
Temperature (°C)
Time (Ma)
Age (Ma) 22
24
26
28
30
32
34
D
Elevation (m)
2700
2600
2500
2400
2300
2200
2
4
6
8
10
12
14
16
MTL (µm)
E Laojun Shan
AFT+AHe
AFT samples
(this study)
JC27 JC30
JC28 JC31
JC29 JC33
AHe samples
(Shen et al., 2016)
L1401 L1410
L1402 L1414
L1403 SG1407
L1404 SG1402
L1407
Thermal reequilibration
Rapid exhumation
Temperature (°C)
Time (Ma)
Age (Ma) 5
10
15
20
25
30
35
F
Elevation (m)
4000
3500
3000
2500
2000
2
4
6
8
10
12
14
16
MTL (µm)
G Shaomao Shan
AFT+AHe
AFT samples
(this study)
CD114
CD117
CD118
CD193
AHe sample
(this study)
CD116
Thermal reequilibration
Rapid exhumation
Temperature (°C)
Time (Ma)
Age (Ma) 20
25
30
35
H
Obs.
Pred.
AHe
AFT
MTL
Elevation (m)
2700
2600
2500
2400
2300
2200
2
4
6
8
10
12
14
16
MTL (µm)

Figure 7.

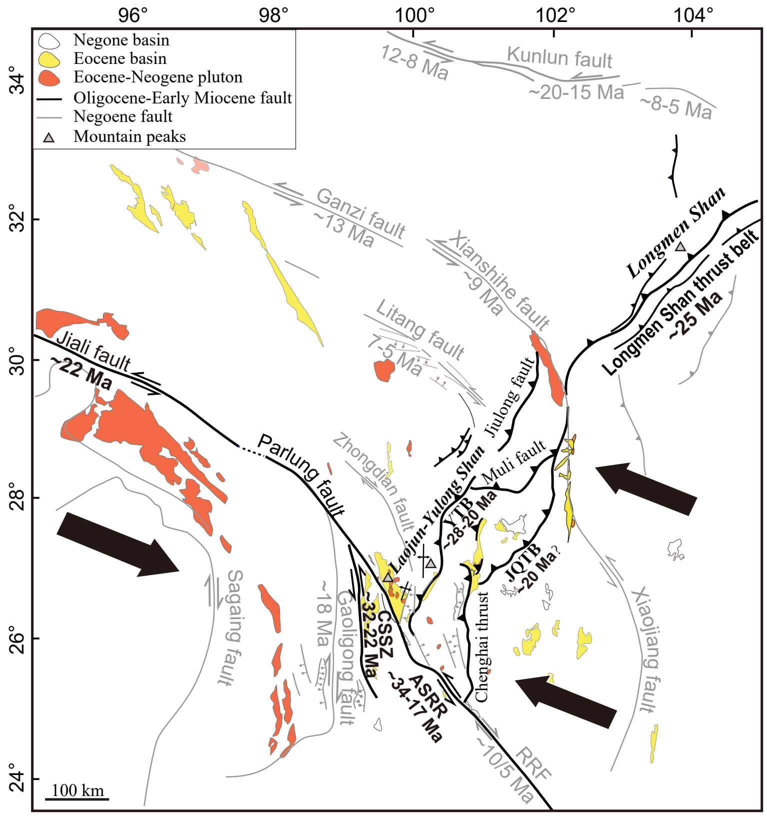
96°
98°
100°
102°
104°
34°
32°
30°
28°
26°
24°
Negone basin
Eocene basin
Eocene-Neogene pluton
Oligocene-Early Miocene fault
Negoene fault
Mountain peaks
12-8 Ma
Kunlun fault
~20-15 Ma
~8-5 Ma
Ganzi fault
~13 Ma
Xianshihe fault
~9 Ma
Longmen Shan
Longmen Shan thrust belt
~25 Ma
Litang fault
7-5 Ma
Jiali fault
~22 Ma
Jiulong fault
Muli fault
Parlung fault
Zhongdian fault
Haba-Yulong Shan
YTB
~28-20 Ma
JQTB
~20 Ma?
Chenghai thrust
Xiaojiang fault
Sagaing fault
~18 Ma
Gaoligong fault
CSSZ
~32-22 Ma
ASRR
~34-17 Ma
RRF
~10/5 Ma
100 km

Reference

Annen, C. (2011), Implications of incremental emplacement of magma bodies for magma differentiation, thermal aureole dimensions and plutonism–volcanism relationships, *Tectonophysics*, 500(1), 3-10.

Braun, J., P. van der Beek, and G. Batt (2006), Quantitative Thermochronology: Numerical methods for the interpretation of thermochronological data, Cambridge University Press, Cambridge, 217 pp.

Burchfiel, B. C., Z.L. Chen, Y.P. Liu, and L. H. Royden (1995), Tectonics of the Longmen Shan and adjacent regions, Central China, *International Geology Review*, 37(8), 661-735.

Bureau of Geology and Mineral Resources of Yunnan Province (BGMRY) (1990), Regional Geology of Yunnan Province, Bureau of Geology and Mineral Resources of Yunnan Province, Beijing, 178 pp.

Cao, S., J. Liu, B. Leiss, A. Vollbrecht, J. Genser, F. Neubauer, and C. Zhao (2011), Initiation of left-lateral deformation along the Ailao Shan-Red River shear zone: new microstructural, textural, and geochronological constraints from the Diancang Shan metamorphic massif, SW Yunnan, China, *International Geology Review*, 54(3), 348-367.

Clark, M. K., M. A. House, L. H. Royden, K. X. Whipple, B. C. Burchfiel, X. Zhang, and W. Tang (2005a), Late Cenozoic uplift of southeastern Tibet, *Geology*, 33(6), 525-528.

Clark, M. K., J. W. M. Bush, and L. H. Royden (2005b), Dynamic topography produced by lower crustal flow against rheological strength heterogeneities bordering the Tibetan Plateau, *Geophysical Journal International*, 162(2), 575-590.

Clark, M. K., L. H. Royden, K. X. Whipple, B. C. Burchfiel, X. Zhang, and W. Tang (2006), Use of a regional, relict landscape to measure vertical deformation of the eastern Tibetan Plateau, *J. Geophys. Res.*, *111*(F3), F3002.

Clark, M. K., and L. H. Royden (2000), Topographic ooze: Building the eastern margin of Tibet by lower crustal flow, *Geology*, 28(8), 703-706.

Clark, M. K., L. M. Schoenbohm, L. H. Royden, K. X. Whipple, B. C. Burchfiel, X. Zhang, W. Tang, E. Wang, and L. Chen (2004), Surface uplift, tectonics, and erosion of eastern Tibet from large-scale drainage patterns, *Tectonics*, 23(1), TC1006, doi: 10.1029/2002tc001402.

Clift, P. D., J. Blusztajn, and A. D. Nguyen (2006), Large-scale drainage capture and surface uplift in eastern Tibet–SW China before 24 Ma inferred from sediments of the Hanoi Basin, Vietnam, *Geophysical Research* Lett*ers*, 33(19), L19403.

Clift, P. D. (2006), Controls on the erosion of Cenozoic Asia and the flux of clastic sediment to the ocean, *Earth and Planetary Science Letters*, 241(3), 571-580.

Deng, B., S. Liu, L. Jiang, G. Zhao, R. Huang, Z. Li, J. Li, and L. Jansa (2017), Tectonic uplift of the Xichang Basin (SE Tibetan Plateau) revealed by structural geology and thermochronology data, *Basin Research*, 30(1), 75-96.

Donelick, R. A., P. B. O'Sullivan, and R. A. Ketcham (2005), Apatite fission-track analysis, *Reviews in Mineralogy and Geochemistry*, 58(1), 49-94.

Duvall, A. R., M. K. Clark, E. Kirby, K. A. Farley, W. H. Craddock, C. Li, and D.-Y. Yuan (2013), Low-temperature thermochronometry along the Kunlun and Haiyuan Faults, NE Tibetan Plateau: Evidence for kinematic change during late-stage orogenesis, *Tectonics*, 32(5), 1190-1211, doi:10.1002/tect.20072.

Ehlers, T. A. (2005), Crustal thermal processes and the interpretation of thermochronometer data, *Reviews in Mineralogy and Geochemistry*, 58(1), 315-350.

Farley, K. A. (2002), (U-Th)/He dating: Techniques, calibrations, and applications, *Reviews in Mineralogy and Geochemistry*, 47(1), 819-844.

Fitzgerald, P. G., and A. J. W. Gleadow (1990), New approaches in fission track geochronology as a tectonic tool: Examples from the transantarctic mountains, *International Journal of Radiation Applications and*

Instrumentation. Part D. Nuclear Tracks and Radiation Measurements, 17(3), 351-357.

Fitzgerald, P. G., R. B. Sorkhabi, T. F. Redfield, and E. Stump (1995), Uplift and denudation of the central Alaska Range: A case study in the use of apatite fission track thermochronology to determine absolute uplift parameters, *Journal of Geophysical Research*, 100(B10), 20175-20191, doi: 10.1029/95JB02150.

Galbraith, R. F., and P. F. Green (1990), Estimating the component ages in a finite mixture, *International Journal of Radiation Applications and Instrumentation. Part D. Nuclear Tracks and Radiation Measurements* , 17(3), 197-206.

Gallagher, K. (2012), Transdimensional inverse thermal history modeling for quantitative thermochronology, *Journal of Geophysical Research*, 117(B2), doi: 10.1029/2011JB008825.

Gautheron, C., L. Tassan-Got, J. Barbarand, and M. Pagel (2009), Effect of alpha-damage annealing on apatite (U-Th)/He thermochronology, *Chemical Geology*, *266*(3), 157-170.

Gleadow, A. J. W., I. R. Duddy, and J. F. Lovering (1983), Fission track analysis: A new tool for the evaluation of thermal histories and hydrocarbon potential, *The APPEA Journal*, 23(1), 93-102.

Godard, V., R. Pik, J. Lavé, R. Cattin, B. Tibari, J. de Sigoyer, M. Pubellier, and J. Zhu (2009), Late Cenozoic evolution of the central Longmen Shan, eastern Tibet: Insight from (U-Th)/He thermochronometry, *Tectonics*, 28(5), doi:10.1029/2008TC002407.

Gourbet, L., P. H. Leloup, J.-L. Paquette, P. Sorrel, G. Maheo, G. Wang, Y. Xu, K. Cao, P.-O. Antoine, I. Eymard, W. Liu, H. Lu, A. Replumaz, M.-L. Chevalier, K. Zhang, J. Wu, and T. Shen (2017), Reappraisal of the Jianchuan Cenozoic basin stratigraphy and its implications on the SE Tibetan plateau evolution, *Tectonophysics*, 700-701, 162-179.

Hoke, G. D., J. Liu-Zeng, M. T. Hren, G. K. Wissink, and C. N. Garzione (2014), Stable isotopes reveal high southeast Tibetan Plateau margin since the Paleogene, *Earth and Planetary Science Letters*, 394, 270-278.

Jolivet, M., M. Brunel, D. Seward, Z. Xu, J. Yang, J. Malavieille, F. Roger, A. Leyreloup, N. Arnaud, and C. Wu (2003), Neogene extension and volcanism in the Kunlun Fault Zone, northern Tibet: New constraints on the age of the Kunlun Fault, *Tectonics*, 22(5), 1052, doi: 10.1029/2002tc001428 %/agu.

Ketcham, R. A., A. Carter, R. A. Donelick, J. Barbarand, and A. J. Hurford (2007), Improved modeling of fission-track annealing in apatite, *American Mineralogist*, 92(5-6), 799-810.

Lacassin, R., U. Scharer, P. H. Leloup, N. Arnaud, P. Tapponnier, X. Liu, and L. Zhang (1996), Tertiary deformation and metamorphism SE of Tibet: The folded Tiger-leap decollement of NW Yunnan, China, *Tectonics*, 15(3), 605-622, doi: 10.1029/95tc03749.

Lee, H. Y., S. L. Chung, J. R. Wang, D. J. Wen, C. H. Lo, T. F. Yang, Y. Zhang, Y. Xie, T. Y. Lee, G. Wu, and J. Ji (2003), Miocene Jiali faulting and its implications for Tibetan tectonic evolution, *Earth and Planetary Science Letters*, 205(3-4), 185-194.

Leloup, P. H., N. Arnaud, R. Lacassin, J. R. Kienast, T. M. Harrison, T. T. P. Trong, A. Replumaz, and P. Tapponnier (2001), New constraints on the structure, thermochronology, and timing of the Ailao Shan-Red River shear zone, SE Asia, *Journal of Geophysical Research*, 106(B4), 6683-6732.

Leloup, P. H., T. M. Harrison, F. J. Ryerson, W. Chen, Q. Li, P. Tapponnier, and R. Lacassin (1993), Structural, Petrological and Thermal Evolution of a Tertiary Ductile Strike-Slip Shear Zone, Diancang Shan, Yunnan, *Journal of Geophysical Research*, *98*(B4), 6715-6743.

Leloup, P. H., R. Lacassin, P. Tapponnier, U. Scharer, D. Zhong, X. Liu, L. Zhang, S. Ji, and P. T. Trinh (1995), The Ailao Shan-Red River shear zone (Yunnan, China), Tertiary transform boundary of Indochina, *Tectonophysics*, 251(1-4), 3-84.

Li, S., B. S. Currie, D. B. Rowley, and M. Ingalls (2015), Cenozoic paleoaltimetry of the SE margin of the Tibetan

Plateau: Constraints on the tectonic evolution of the region, *Earth and Planetary Science Letters*, 432, 415-424.

Lin, T. H., C. H. Lo, S. L. Chung, F. J. Hsu, M. W. Yeh, T. Y. Lee, J. Q. Ji, Y. Z. Wang, and D. Liu (2009), ^{40}Ar/^{39}Ar dating of the Jiali and Gaoligong shear zones: Implications for crustal deformation around the Eastern Himalayan Syntaxis, *Journal of Asian Earth Sciences*, 34(5), 674-685.

Liu-Zeng, J., P. Tapponnier, Y. Gaudemer, and L. Ding (2008), Quantifying landscape differences across the Tibetan plateau: Implications for topographic relief evolution, *Journal of Geophysical Research*, 113(F04018), doi:10.1029/2007JF000897.

Liu-Zeng, J., J. Zhang, D. McPhillips, P. Reiners, W. Wang, R. Pik, L. Zeng, G. Hoke, K. Xie, P. Xiao, D. Zheng, and Y. Ge (2018), Multiple episodes of fast exhumation since Cretaceous in southeast Tibet, revealed by low-temperature thermochronology, *Earth and Planetary Science Letters*, *490*, 62-76.

Lu, Y.J., R. Kerrich, P. A. Cawood, T. C. McCuaig, C. J. R. Hart, Z. X. Li, Z.Q. Hou, and L. Bagas (2012), Zircon SHRIMP U-Pb geochronology of potassic felsic intrusions in western Yunnan, SW China: Constraints on the relationship of magmatism to the Jinsha suture, *Gondwana Research*, 22(2), 737-747.

McPhillips, D., G. D. Hoke, J. Liu-Zeng, P. R. Bierman, D. H. Rood, and S. Niedermann (2016), Dating the incision of the Yangtze River gorge at the First Bend using three-nuclide burial ages, *Geophysical Research Letters*, 43(1), 101-110.

Murray, K. E., P. W. Reiners, and S. N. Thomson (2016), Rapid Pliocene-Pleistocene erosion of the central Colorado Plateau documented by apatite thermochronology from the Henry Mountains, *Geology*, 44(6), 483-486.

Nie, J. et al. (2018), Rapid incision of the Mekong River in the middle Miocene linked to monsoonal precipitation, *Nature Geoscience*, 102, doi:10.1038/s41561-018-0244-z.

Ouimet, W., K. Whipple, L. Royden, P. Reiners, K. Hodges, and M. Pringle (2010), Regional incision of the eastern margin of the Tibetan Plateau, *Lithosphere*, 2(1), 50-63.

Palin, R. M., M. P. Searle, D. J. Waters, R. R. Parrish, N. M. W. Roberts, M. S. A. Horstwood, M. W. Yeh, S. L. Chung, and T. T. Anh (2013), A geochronological and petrological study of anatectic paragneiss and associated granite dykes from the Day Nui Con Voi metamorphic core complex, North Vietnam: constraints on the timing of metamorphism within the Red River shear zone, *Journal of Metamorphic Geology*, 31(4), 359-387.

Perrineau, A. (2010), Evolution morphologique et tectonique récente des marges NE et SE du plateau tibétain: lien avec la dynamique des grands fleuves, 421 pp, Institut de Physique du Globe de Paris.

Reiners, P. W., and M. T. Brandon (2006), Using thermochronology to understand orogenic erosion, *Annual Review of Earth and Planetary Sciences*, 34(1), 419-466.

Replumaz, A., R. Lacassin, P. Tapponnier, and P. H. Leloup (2001), Large river offsets and Plio-Quaternary dextral slip rate on the Red River fault (Yunnan, China), *Journal of Geophysical Research*, 106(B1), 819-836, doi:10.1029/2000JB900135.

Richardson, N. J., A. L. Densmore, D. Seward, A. Fowler, M. Wipf, M. A. Ellis, L. Yong, and Y. Zhang (2008), Extraordinary denudation in the Sichuan Basin: Insights from low-temperature thermochronology adjacent to the eastern margin of the Tibetan Plateau, *Journal of Geophysical Research*, 113(B4), doi:10.1029/2006JB004739.

Royden, L. H., B. C. Burchfiel, R. W. King, E. Wang, C. Zhiliang, S. Feng, and L. Yuping (1997), Surface deformation and lower crustal flow in eastern Tibet, *Science*, 276(5313), 788-790.

Schärer, U., Zhang, L. S., and Tapponnier, P. (1994). Duration of strike-slip movements in large shear zones: the Red River belt, China. *Earth and Planetary Science Letters*, 126(4), 379-397.

Schoenbohm, L. M., B. C. Burchfiel, and C. Liangzhong (2006), Propagation of surface uplift, lower crustal flow, and Cenozoic tectonics of the southeast margin of the Tibetan Plateau, *Geology*, 34(10), 813 -816.

Shen, X., Y. Tian, D. Li, S. Qin, P. Vermeesch, and J. Schwanethal (2016), Oligocene-Early Miocene river incision near the first bend of the Yangze River: Insights from apatite (U-Th-Sm)/He thermochronology, *Tectonophysics*, 687, 223-231.

Tang, M., J. Liu-Zeng, G. D. Hoke, Q. Xu, W. Wang, Z. Li, J. Zhang, and W. Wang (2017), Paleoelevation reconstruction of the Paleocene-Eocene Gonjo basin, SE-central Tibet, *Tectonophysics*, 712-713, 170-181.

Tapponnier, P., G. Peltzer, A. Y. Le Dain, R. Armijo, and P. Cobbold (1982), Propagating extrusion tectonics in Asia: New insights from simple experiments with plasticine, *Geology*, 10(12), 611-616.

Tapponnier, P., Z .Q. Xu, F. Roger, B. Meyer, N. Arnaud, G. Wittlinger, and Y. Jingsui (2001), Oblique stepwise rise and growth of the Tibet Plateau, *Science*, 294(5547), 1671.

Tian, Y., B. P. Kohn, A. J. W. Gleadow, and S. Hu (2014), A thermochronological perspective on the morphotectonic evolution of the southeastern Tibetan Plateau, *Journal of Geophysical Research*, 119(1), 2013JB010429, doi:10.1002/2013jb010429.

Tian, Y., B. P. Kohn, S. Hu, and A. J. W. Gleadow (2015), Synchronous fluvial response to surface uplift in the eastern Tibetan Plateau: Implications for crustal dynamics, *Geophysical Research Letters*, 42(1), doi: 2014GL062383.

Wang, J, and S. Huang (1988). Compilation of heat flow data in the continental area of China. *Scientia Geologica Sinica*, 2, 196-204.

Wang, E., B. C. Burchfiel, L. H. Royden, L. Chen, J. Chen, W. Li, and Z. Chen (1998), Late Cenozoic Xianshuihe-Xiaojiang, Red River, and Dali Fault Systems of Southwestern Sichuan and Central Yunnan, China, *Geological Society of America Special Papers*, 327, 1-108.

Wang, E., E. Kirby, K. P. Furlong, M. van Soest, G. Xu, X. Shi, P. J. J. Kamp, and K. V. Hodges (2012a), Two-phase growth of high topography in eastern Tibet during the Cenozoic, *Nature Geoscience*, 5(9), 640-645.

Wang, S., X. Fang, D. Zheng, and E. Wang (2009), Initiation of slip along the Xianshuihe fault zone, eastern Tibet, constrained by K/Ar and fission-track ages, *International Geology Review*, 51(12), 1121-1131.

Wang, S., G. Jiang, T. Xu, Y. Tian, D. Zheng, and X. Fang (2012b), The Jinhe-Qinghe fault-An inactive branch of the Xianshuihe-Xiaojiang fault zone, Eastern Tibet, *Tectonophysics*, 544-545, 93-102.

Wilson, C. J. L., and A. P. Fowler (2011), Denudational response to surface uplift in east Tibet: Evidence from apatite fission-track thermochronology, *Geological Society of America Bulletin*, 123(9-10), 1966 -1987.

Wissink, G. K., G. D. Hoke, C. N. Garzione, and J. Liu-Zeng (2016), Temporal and spatial patterns of sediment routing across the southeast margin of the Tibetan Plateau: Insights from detrital zircon, *Tectonics*, 35(11), 2538-2563.

Xu, G., and P. J. J. Kamp (2000), Tectonics and denudation adjacent to the Xianshuihe Fault, eastern Tibetan Plateau: Constraints from fission track thermochronology, *Journal of Geophysical Research*, 105(B8), 19231-19251.

Yan, B., A. Lin, 2015. Systematic deflection and offset of the Yangtze River drainage system alongthe strike-slip Ganzi–Yushu–Xianshuihe Fault Zone, Tibetan Plateau. *Journal of Geodynamics*. 87, 13–25.

Yang, Z., C. Shen, L. Ratschbacher, E. Enkelmann, R. Jonckheere, B. Wauschkuhn, and Y. Dong (2017), Sichuan Basin and beyond: Eastward foreland growth of the Tibetan Plateau from an integration of Late Cretaceous-Cenozoic fission track and (U-Th)/He ages of the eastern Tibetan Plateau, Qinling, and Daba Shan, *Journal of Geophysical Research*, 122(6), 4712-4740, doi:10.1002/2016JB013751.

Zhang, B., J. Zhang, and D. Zhong (2010), Structure, kinematics and ages of transpression during strain-partitioning in the Chongshan shear zone, western Yunnan, China, *Journal of Structural Geology*, 32(4), 445-463.

Zhang, B., J. Zhang, Z. Chang, X. Wang, F. Cai, and Q. Lai (2012), The Biluoxueshan transpressive deformation zone monitored by synkinematic plutons, around the Eastern Himalayan Syntaxis, *Tectonophysics*, 574-575, 158-180.

Zhang, H., M. E. Oskin, J. Liu-Zeng, P. Zhang, P. W. Reiners, and P. Xiao (2016), Pulsed exhumation of interior eastern Tibet: Implications for relief generation mechanisms and the origin of high-elevation planation surfaces, *Earth and Planetary Science Letters*, 449, 176-185.

Zhang, Y. Z., A. Replumaz, P. H. Leloup, G. C. Wang, M. Bernet, P. van der Beek, J. L. Paquette, and M. L. Chevalier (2017), Cooling history of the Gongga batholith: Implications for the Xianshuihe Fault and Miocene kinematics of SE Tibet, *Earth and Planetary Science Letters*, 465, 1-15.

Zhang, Y. Z., A. Replumaz, G. C. Wang, P. H. Leloup, C. c. Gautheron, M. Bernet, P. van der Beek, J. L. Paquette, A. Wang, K. X. Zhang, M. L. Chevalier, and H. B. Li (2015), Timing and rate of exhumation along the Litang fault system, implication for fault reorganization in Southeast Tibet, *Tectonics*, 34(6), 2014TC003671, doi:10.1002/2014tc003671.